CHALMERS
UNIVERSITY OF TECHNOLOGY

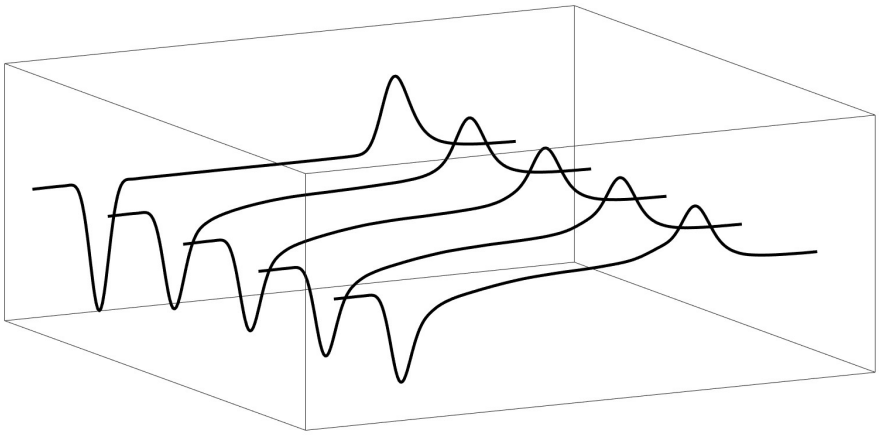

Characterization of the Pulsed Electro-Acoustic Method in HVDC Materials

Investigating the Influence of Electrode Configurations and Acoustic Coupling Media on the Space Charge Accumulation using the Pulsed Electro-Acoustic Method

Master's Thesis in Electrical Engineering

TOM SANDRÉN

DEPARTMENT OF ELECTRICAL POWER ENGINEERING

CHALMERS UNIVERSITY OF TECHNOLOGY
Gothenburg, Sweden 2026
www.chalmers.se

Master's Thesis 2026

Characterization of the Pulsed Electro-Acoustic Method in HVDC Materials

Investigating the Influence of Electrode Configurations and Acoustic Coupling Media on the Space Charge Accumulation using the Pulsed Electro-Acoustic Method

TOM SANDRÉN

CHALMERS
UNIVERSITY OF TECHNOLOGY

Department of Electrical Power Engineering
Chalmers University of Technology
Gothenburg, Sweden 2026

Characterization of the Pulsed Electro-Acoustic Method in HVDC Materials
Investigating the Influence of Electrode Configurations and Acoustic Coupling Media on the Space Charge Accumulation using the Pulsed Electro-Acoustic Method
Tom Sandrén

Supervisors:
Johan Andersson, Borouge International
Ramona Huuva, Borouge International
Xiangdong Xu, Department of Electric Power Engineering
Examiners:
Yuriy Serdyuk, Department of Electrical Power Engineering
Dan Kuylenstierna, Department of Microtechnology and Nanoscience

Master's Thesis 2026
Department of Electrical Power Engineering
Chalmers University of Technology
SE-412 96 Gothenburg
Sweden
Telephone +46 31 772 1000

Cover: Time evolution of the space charge density captured using the Pulsed Electro-Acoustic method.

Typeset in LaTeX
Gothenburg, Sweden 2026

Characterization of the Pulsed Electro-Acoustic Method in HVDC Materials
Investigating the Influence of Electrode Configurations and Acoustic Coupling Media on the Space Charge Accumulation using the Pulsed Electro-Acoustic Method

Tom Sandrén
Department of Electrical Power Engineering
Chalmers University of Technology

Abstract

The Pulsed Electro-Acoustic (PEA) method is a non-destructive technique used to measure space charge accumulation in polymeric insulation materials used for extruded high voltage direct current (HVDC) power cables. However, the measured space charge profiles are sensitive to the measurement setup. In this work, the influence of electrode configurations and acoustic coupling media (ACM) on PEA measurements has been investigated using commercial grade HVDC cross-linked polyethylene (XLPE) materials supplied by Borouge International. PEA measurements were performed using four different electrode configurations to assess the influence of semiconductive and metallized interfaces on charge injection and space charge accumulation. The measurements were conducted at two electric field strengths and two temperatures. In addition, three acoustic coupling media were evaluated based on a pre-screening procedure. The results show that the electrode configuration has a significant impact on the space charge profile of the XLPE insulation. Configurations utilizing metallized semiconductive electrodes reduced the overall charge injection compared to configurations using semiconductive electrodes without metallization. When the electrodes were sputtered direcetly onto the XLPE insulation, the influence of both the semiconductive electrode and the acoustic coupling medium was decoupled from the insulation sample, therefore reflecting the intrinsic space charge dynamics of the XLPE insulation. The acoustic coupling media were also found to influence the measurements. One of the acoustic coupling medium tested was observed to migrate into both the XLPE insulation and the XLPE semiconductive electrode materials, resulting excessive material swelling at 70 °C. Acoustic coupling media with higher viscosity was found to increase overall homocharge injection at 25 °C, and contribute to heterocharge accumulation at the high voltage electrode at 70 °C, indicating increased Maxwell-Wagner polarization at the ACM-insulation interface.

Keywords: Space Charge, Charge Injection, Charge Accumulation, PEA, HVDC Materials, Acoustic Coupling Media

Acknowledgements

First and foremost, I want to thank Borouge International for giving me the opportunity to do this project, combining many interesting disciplines all at once.

Also, I want to thank my examiner Yuriy Serdyuk and supervisor Xiangdong Xu at Chalmers for always keeping me grounded and making sure to be aware of my progress throughout the entire process.

A special thanks to my supervisor at Borouge International Johan Andersson for your immense encouragement, guidance and highly rewarding discussions. Your deep knowledge and interest in the field of cable insulation materials has been very inspiring throughout the entire process.

A big thanks to Nilena Andersson, Martin Macken, Annika Smedberg and my second supervisor at Borouge International Ramona Huuva, for all of the interesting discussions and continuous encouragement throughout this project.

Tom Sandrén, Gothenburg, May 2026

List of Acronyms

Below is the list of acronyms that have been used throughout this thesis listed in alphabetical order:

ACM	Acoustic Coupling Medium
DC	Direct Current
FEF	Field Enhancement Factor
HV	High Voltage
HVAC	High Voltage Alternating Current
HVDC	High Voltage Direct Current
PE	Polyethylene
PEA	Pulsed Electro-Acoustic
PVDF	Polyvinylidenefluoride
XLPE	Cross-linked Polyethylene

Contents

List of Figures

List of Tables

1
Introduction

1.1 Background

In recent years power transmission using high voltage direct current (HVDC) has become more competitive compared to power transmission relying on high voltage alternate current (HVAC). This is especially the case for long haul power transmission. In contrast to HVAC cables, there is no physical restriction that limits the cable lengths for HVDC cables [1].

For a given conductor cross section, the line losses for HVDC cables can be roughly half of the line losses of HVAC cables [1]. Compared to power transmission utilizing HVDC, HVAC transmits both active and reactive power. Because of the reactive component in HVAC power transmission, there will be a drop off in power transmission capacity compared to HVDC power transmission [1, 2]. The reactive power consumed by long HVAC cables would, without sufficient compensation of shunt reactances, inhibit transmission of active power [3]. This makes HVAC systems unpractical, especially for long haul sea-links [2].

Furthermore, HVDC cables can be divided into two categories based on the type of insulation used. These two types are: mass-impregnated (MI) insulation; and extruded insulation [3]. However, the manufacturing process for MI insulated cables are rather complex and expensive [4]. In addition, HVDC cables utilizing extruded insulation can withstand higher operating temperatures compared to power cables utlizing MI insulation. Traditional MI cables have a temperature limit of around 55 °C, whereas the temperature limit of extruded cross-linked polyethylene (XLPE) cables are roughly 90 °C [2, 3].

The HVDC cable market has been dominated by MI insulated cables up until the mid 1990s [2]. Since then, extended research has been put into replacing MI insulation with extruded insulation. The cable types using extruded insulation are based on polymeric materials, mostly consisting of polyethylene (PE) [5].

The first prototype HVDC cables utlizing PE insulation where found to fail prematurely at the operating voltage [4]. In addition, the early extruded PE cables were also found to be weakened when after polarity reversal [6]. The main reason for why these cables failed was due to space charge accumulation within the PE insulation [2].

Even though the extruded insulation appears to be homogeneous, there may be regions within the material where additives and/or by-products are still present [7]. This may in turn exacerbate the accumulation of space charge within the insulating material [2]. Additionally, space charge accumulation within the cable insulation may in turn give rise to an enhancement of the electric field inside the insulation, which has shown to affect the longevity of extruded HVDC cables [7, 8]. The first HVDC power transmission system that successfully utilized cables with extruded insulation was in the Swedish island Gotland [9].

As mentioned above, the failed attempts to introduce cable systems utilizing extruded insulation was primarily due to space charge accumulation within the cable insulation. This resulted in a strong demand for finding ways to measure the space charge distributions within the insulation material [8]. Since the 1970s, several non-destructive ways to measure space charge within dielectric materials have been demonstrated [8, 10].

Non-destructive methods for measuring the space charge distributions within dielectric materials can be divided into two categories, namely: thermal methods; and acoustic methods [10]. The latter measurement category, in which this thesis will be based upon, includes the pulsed electro-acoustic (PEA) method.

1.1.1 The Pulsed Electro-Acoustic (PEA) Method

One of the most popular non-destructive techniques used to measure the space charge distributions in materials used for high voltage insulation is the PEA method [8]. The PEA method measures the spatial charge distribution of within the bulk by converting the interaction between a high voltage pulse and the internal space charge distribution into a pressure wave that propagates through the dielectric material.

In a PEA measurement a DC voltage is applied across the sample, subjecting it to an external electric field. Short nanosecond high voltage pulses are superimposed onto the external field, which in turn interact with the charges inside the material and generates a transient pressure wave [11]. This acoustic wave originates from three main sources: the surface charges induced at the ground electrode; the surface charges at the high voltage electrode; and the space charge distributed within the bulk [8].

Furthermore, the generated pressure wave propagates through the sample and reaches a piezoelectric transducer attached to the ground electrode [12]. The transducer converts the mechanical pressure into a time varying electrical voltage signal. Since the speed of sound in the sample as well as its thickness are known quantities, the internal space charge profile can be reconstructed through signal processing of the time dependent electrical signal [8, 11, 13]. A description of the PEA circuit is presented in Appendix A.0.1, and the PEA measurement principle is provided in Appendix A.0.2.

1.2 Aim

The aim of this thesis is to contribute to the development of more reliable PEA measurements by proper choice of electrodes and acoustic coupling media. When testing and evaluating insulating materials for HVDC applications, it is of most importance to understand how common types of electrodes influence the charge injection properties.

In part, this work aims to assess how various electrode configurations affects the space charge accumulation in the polymeric insulating material used for HVDC cables. Moreover, by altering the influence the semiconductive electrode material, this work aims to find new methods for evaluating whether the accumulation of space charge is intrinsic to the insulating material itself, or if it is due to the charge injection from the electrode screen material (i.e., the semiconductive electrode). Also, this work aims to assess how different acoustic coupling media affects the PEA measurements.

To this end, this work aims to achieve this by answering the following questions:

1. How do different electrode configurations influence the charge injection and the resulting space charge accumulation?
2. What influence does different types of acoustic coupling media have on the space charge measurements, as well as on the materials themselves in terms of space charge accumulation?
3. To what extent does the observed differences in space charge accumulation stem from the measurement setup, rather than intrinsic material properties?

1.3 Limitations

This work will limited to one specific type of cross-linked polyethylene (XLPE) insulation material and one specific type of XLPE semiconductive material provided by Borouge International for all PEA measurement. The PEA measurements conducted in this work is also limited to two electric field strengths, performed at two different temperatures. In addition, this work is aimed towards measurement techniques and trying to understand how, and to what extent, different electrode configurations and acoustic coupling media influence the space charge dynamics in HVDC insulation materials to further the understanding of what is actually being measured when using the PEA method. Therefore, due to the sparse material selection, the results presented herein cannot draw general conclusions about specific material properties, but rather as a guideline into how different measurement setups influence the outcome of the PEA measurements to better understand what is being measured.

2
Theory

In this chapter, relevant theory to describe the physical phenomena observed in the results is presented. The chapter starts out by explaining the electrostatics in dielectic materials, with an emphasis on Poisson's equation. In later sections the theory of charge generation and conduction mechanisms in polymeric materials are outlined.

2.1 Electrostatics in Dielectric Materials

When a static electric field is applied across a dielectic material, the material behaves differently from that of a conductive material [14]. Since charge carriers are not free to move inside the dielectic material, the applied field primarily causes a redistribution of bound charges within the material resulting in polarization. However, under certain conditions free charges may appear within dielectic materials due to processes such as charge injection from the electrodes or trapping and de-trapping of charge carriers [7, 8].

The electric field distribution inside a dielectric material is governed by Gauss's law [7], which relates the divergence of the electric field and the local charge density. This relationship is given by

$$\nabla \cdot (\varepsilon \mathbf{E}) = \rho, \tag{2.1}$$

where $\mathbf{E}$ is the electric field, ρ is the charge density, and ε is the permittivity of the dielectric material. The permittivity, ε, is often expressed as the product of the permittivity of free space ($\varepsilon_0 = 8.854 \cdot 10^{-12}$ F m^{-1}) and the relative permittivity, ε_r, of the material. Furthermore, the electric field is defined as the negative gradient of the electric potential

$$\mathbf{E} = -\nabla V, \tag{2.2}$$

where V is the electric potential. Substituting Equation (2.2) into (2.1), assuming non-varying permittivity within the dielectric, yields Poisson's equation, providing a mathematical relationship between the electric potential and the charge density

$$\nabla^2 V = -\frac{\rho}{\varepsilon}. \tag{2.3}$$

Poisson's equation given in (2.3) shows that the spatial distribution of electrical potential inside a dielectric is determined by the charge density within the bulk. In

the absence of internal charges within the material, the charge density is zero which reduces Poisson's equation given in (2.3) to Laplace's equation

$$\nabla^2 V = 0. \tag{2.4}$$

In this case, the electric field distribution is reduced to a boundary value problem. That is, the electric field distribution is solely determined by the applied voltage at the electrodes.

From Poisson's equation in (2.3), there is a spatial variation in the electric potential within the material. This implies that the presence of internal charges within the material may cause distortions in the internal electric field distribution within the dielectric material.

2.1.1 Homo- and Heterocharges

For dielectric materials subjected to an external uniform electric field E_0, two types of space charge distributions can be observed near the electrodes. Depending on the polarity of the space charge relative to the adjacent electrode, these charges are commonly referred to as homocharge and heterocharge [14].

Homocharge refers to charge carriers that have the same polarity as the electrode at which they are accumulated [14]. For example, a charge accumulation with negative polarity near the cathode constitutes a homocharge. Moreover, homocharge are typically injected charges that gets trapped. This mechanism often occurs when the charge injection from the electrodes are greater than the charge transport within the bulk [2]. Homocharge present in the vicinity of the electrodes tends to screen the external electric field near the electrodes. Hence inside the bulk, the electric field will be lower than the applied field E_0 near the electrodes and higher in the bulk [2, 7].

In contrast, heterocharge refers to charge carriers that whose polarity is opposite to that of the adjacent electrode. Accumulation of heterocharge occur when the charge transport is greater than the charge injection [7]. Accumulation of heterocharge will enhance the electric field near the electrodes and reduce the electric field inside the bulk of the dielectric [2, 8].

2.1.2 Space Charges

More generally, any accumulation of charge within a dielectric material is referred to as space charge. As stated previously, these internal charges may extend throughout the bulk of the material and can lead to substantial distortion of the internal electric field compared to the externally applied electric field.

A part from homo- and heterocharge near the electrodes, charge may also accumuluate throughout the bulk of the material. The accumulation of space charge may in turn cause local regions of electrical stress due to enhancement of the local electric field [8]. As a consequence, the local field enhancements may contribute to electric field strengths that exceeds the breakdown strength of the material [7].

2.2 Charge Generation in Polymeric Insulation Materials

In polymeric insulation materials used in HVDC cables, there are two main mechanisms of charge generation within the insulation material. The fist one being internal charge and the latter being charge injection. Internal charges are mainly formed from dislocations, impurities, ionic additives and other chemical defects. Charge injection is a phenomenon that occurs at the interface between the conductor and the insulation of the HVDC cable. Thus, the mechanisms that drives the charge generation is not only highly dependent on the electrode/dielectric configuration and its resulting band structure, but also on the electric field strength and temperature within the cable system.

2.2.1 Internal Charge Generation

The most commonly used insulation material for commercial HVDC power cables is cross-linked polyethylene (XLPE) [2]. In XLPE insulation materials, the main drivers of the formation of heterocharges inside the insulation is antioxidants, moisture, crosslinking by-products and impurities [2, 15, 16]. According to [15], moisture have been shown to promote ionization of crosslinking by-products in XLPE materials, even at relatively low concentrations.

2.2.2 Charge Injection

In insulation materials used for high voltage cables, such as XLPE, the electrical conduction not only depends on how charges move and behave within the bulk, but also on how they may enter externally. The latter refers to the mechanism known as charge injection and it explains the process in which charge carriers (e.g. electrons and holes) are transferred from the conductor core to the insulating material in HVDC cables [2, 7].

At the interface between a conductor and an insulator there will be a potential barrier that will limit the transfer of charge carriers between the two materials [7]. The nature of this interface, however, is outside the scope of this thesis work. In particular the complexities of the energy band diagrams formed at this types of interfaces.

In XLPE HVDC power cables, charges will be injected into the XLPE insulation material from the conductor shield layer, which is usually comprised of a semiconductive material. At this interface, homocharge will be injected into the insulation material [2].

2.2.2.1 Schottky Injection

The charge injection process HVDC cable systems can be described by two main mechanisms: Schottky injection and Fowler-Nordheim injection. Schottky injection is described by the height of the potential barrier, Φ_D, formed between the conductor/insulator interface. The current density due to Schottky injection can be modelled mathematically as [7]

$$J = \frac{4\pi e m k_B^2 (1-R) T^2}{h^3} \exp\left[-\frac{1}{k_B T}\left(\Phi_D - \sqrt{\frac{e^3 E}{4\pi\varepsilon}}\right)\right], \tag{2.5}$$

where e is the elementary charge, m is the mass of the electron, R is the reflection coefficient, T is the temperature in Kelvin, h is Planck's constant, k_B is Boltzmann's constant, E is the electric field strength and ε is the permittivity of the insulating material. Moreover, the term $4\pi e m k_B^2/h^3$ in Equation (2.5) is the Richardson's constant [2] and it is often denoted as

$$A = \frac{4\pi e m_e k_B^2}{h^3}, \tag{2.6}$$

$$\tag{2.7}$$

which makes the mathematical expression for the Schottky injection more compact, and can thus be expressed as

$$J = A(1-R)T^2 \exp\left[-\frac{1}{k_B T}\left(\Phi_D - \sqrt{\frac{e^3 E}{4\pi\varepsilon}}\right)\right]. \tag{2.8}$$

2.2.2.2 Fowler-Nordheim Injection

The mechanisms driving the Fowler-Nordheim injection is best described though the lens of quantum mechanics. In classical mechanics, a particle with energy E_p cannot overcome a potential barrier with energy V. Due to the wave-particle duality of particles such as electrons, this phenomenon is possible at the quantum level [17]. For a particle exhibiting wave-particle duality with kinetic energy, E_p, there is a finite and non-zero probability for the event that the particle surpasses a region of potential energy V, where $V > E_p$. This phenomenon is known as quantum tunneling [17, 18].

The Fowler-Nordheim charge injection is a quantum tunneling phenomena whereby a charge carrier tunnels through the potential barrier formed at the conductor-insulator interface [19]. Mathematically, the current density due to Fowler-Nordheim injection can be expressed as [7]

$$J = \frac{e^3 E^2}{4\hbar\Phi_D} \exp\left[-\frac{4}{3}\sqrt{\frac{2m}{\hbar}}\left(\frac{\Phi_D^{3/2}}{eE}\right)\right], \tag{2.9}$$

where $\hbar = h/2\pi$ is the reduced Planck's constant.

From both Equations (2.8) and (2.9), charge injection is highly dependent on both temperature and the applied electric field strength. That is to say, the charge injection into the XLPE insulation in a HVDC cable system will increase as the temperature increases or as the electric field increases. However, its worth mentioning that Fowler-Nordheim injection takes place at rather high electric field strengths (typically $>$ 100 kV/mm [7]) and will therefore not be considered in this work.

2.3 Charge Transport in Polymeric Materials

In polymeric insulation materials, the charge transport is mostly driven by the localized states distributed throughout the forbidden gap [20]. These localized states are commonly referred to as charge traps [16]. Charge traps within dielectric materials are characterized by the depth of their potential energy, and they can either be shallow or deep [7]. The charge traps will act as sinks, capturing charges for a certain period of time. For polymeric materials, such as HVDC insulation, the duration for which a charge carrier is trapped within a certain localized state is dependent on its potential energy depth, the temperature, and the applied DC stress [7, 16].

Moreover, a charge carrier trapped in a localized state can be transferred between adjacent localized state by means of hopping. In polymers, the conduction current is primarily driven by the transport of charges between shallow traps. In contrast, charge carriers trapped within localized states with greater energy depth (e.g. deep traps) will result in space charge [16].

2.3.1 The Poole-Frenkel Mechanism and Hopping Transfer

In contrast to the mechanism behind Schottky injection, whereby the barrier height at an electrode-insulator interface is lowered by an externally applied electric field. The Poole-Frenkel mechanism is the bulk equivalent of the aforementioned mechanism [7].

When an external electric field with sufficient field strength is applied it can be shown that the potential of an ionized donor trap site will decrease ΔW from the vacuum level proportional to the square root of the externally applied electric field according to [16]

$$\Delta W \propto \sqrt{E}. \tag{2.10}$$

Hence, at high electric fields the coulombic potential near an ionzied trap site gets reduced, increasing the probability that a trapped electron will either be donated to the conduction band or hopping to a neighboring trap site [7].

Hopping transfer is governed by a thermally assisted tunneling phenomena between localized states [16]. A part from the superimopsed electic field, the probability that a charge carrier will hop to a neighboring state is also dictated by the distance to neighboring states and their energy levels [7]. In polymeric materials for example, electron conduction occurs between low density regions in between the polymer chains [16].

2.3.2 Charge Mobility

In polymeric materials, the spatial movement of charge carriers are often considered to dominated by the hopping mechanism [7] briefly described in Section 2.3.1 above. From the description provided above, the charge carrier mobility, μ, can be shown [16] to be proportional to the temperature and the applied electric field strength according to

$$\mu \propto \frac{2k_BTa}{h} \sinh\left(\frac{eEa}{2k_BT}\right), \tag{2.11}$$

with k_B being the Boltzmann's constant, T being the temperature in Kelvin, a being the average distance between trap sites, h being the Planck's constant, e being the elementary charge, and E being the applied electric field strength.

2.4 Space Charge Accumulation in Polymeric Materials

For polymeric materials, such as polyethylene, subjected to a DC voltage it can be shown [2] that charge will accumulate inside the bulk when there is a spatial gradient in the permittivity/conductivity ratio of the material at steady state in accordance with

$$\rho = \mathbf{J} \cdot \nabla \left(\frac{\varepsilon_0 \varepsilon_r}{\sigma} \right) = \sigma \mathbf{E} \cdot \nabla \left(\frac{\varepsilon_0 \varepsilon_r}{\sigma} \right), \tag{2.12}$$

where ρ is the accumulated space charge, $\mathbf{J}$ is the steady state current density, ε_0 is the permittivity of free space, $\mathbf{E}$ is the applied electric field, ε_r and σ are the relative permittivity and conductivity of the material, respectively.

2.5 Field Enhancement Factor

As mentioned above, accumulated space charge gives rise to locally varying electric field distortions. One way to quantify these locally varying field distortions is through the field enhancement factor. The field enhancement factor for a flat specimen of thickness d can thus be defined as [12]

$$FEF = \frac{E(x)}{E_0} = \frac{E(x)}{\frac{U_0}{d}}, \tag{2.13}$$

where $E(x)$ is the local electric field strength at position x inside the bulk, U_0 is the applied voltage and d is the thickness of the sample.

For a sample subjected to an applied DC stress, the field enhancement factor in Equation (2.13) evaluated at the electrodes (i.e. at position $x = 0$ or $x = d$) provides the following:

- $FEF < 1$: Reduction of the local electric field strength, indicating the presence of homocharge.
- $FEF = 1$: No space charge accumulation (i.e. Laplacian field).
- $FEF > 1$: Enhancement of the local electric field strength, indicating the presence of heterocharge.

2.6 Maxwell-Wagner Interfacial Polarization

Consider the multistucture depicted in Figure 2.1 subjected to a DC voltage U. The structure consists of two dielectric materials with thickness d_1 and d_2, conductivities σ_1 and σ_2 as well as relative permittivities ε_{r1} and ε_{r2}.

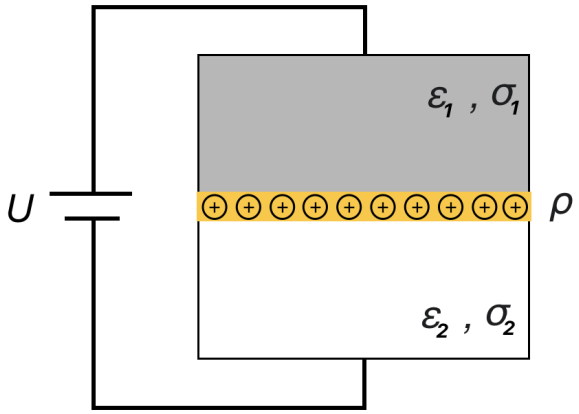

Figure 2.1: Illustration of Maxwell-Wagner interfacial polarization between two dielectric slabs with permittivities ε_1 and ε_2, and conductivities σ_1 and σ_2, subjected to a DC voltage U. Adapted from [21].

When the dielectric structure depicted in Figure 2.1 is subjected to a DC voltage, it has been shown [21] that the saturated charge density at the interface between the two dielectric slabs can be expressed as

$$\rho = \varepsilon_0 \left(\frac{\varepsilon_{r2}\sigma_1 - \varepsilon_{r1}\sigma_2}{d_1\sigma_2 + d_2\sigma_1} \right) U, \tag{2.14}$$

Given the polarity of the DC voltage source depicted in Figure 2.1, the polarity of the accumulated charges at the interface is determined by the mismatch in the permittivity and conductivity of the two dielectric materials. From Equation (2.14), this implies that:

- the accumulated charges will be positive if $\varepsilon_{r1}\sigma_2 < \varepsilon_{r2}\sigma_1$,
- the accumulated charges will be negative if $\varepsilon_{r1}\sigma_2 > \varepsilon_{r2}\sigma_1$,
- no charge accumulation if $\varepsilon_{r1}\sigma_2 = \varepsilon_{r2}\sigma_1$.

3

Methods

This chapter aims to provide a description of the experimental methods used to conduct the the work presented in this thesis. Firstly, in Section 3.1 the sample preparation is described. Secondly, in Section 3.2, the space charge measurement procedure is presented, followed by a short description in 3.2.1 on the signal processing of the signals obtained using the PEA method. Thirdly, in Section 3.3, the four electrode configurations are presented. Lastly, in Sections 3.4 and 3.5, how the acoustic coupling medium were chosen and which were used to conduct this work is presented.

3.1 Sample Preparation

In the following section, the sample preparation is outlined. For all the PEA measurements carried out in this work, two different XLPE materials were used: a semiconductive material (*Semicon*) used as an electrode in the PEA measurements and a high voltage insulation material (*Insulation*). Both the semicon and insulation were commercial grade XLPE material produced by Borouge International for use in extruded HVDC power cables.

3.1.1 Thin Plaques

Firstly, the semiconductive electrode and the insulation samples were compression molded from pellets into plaques with a diameter of 26 cm and a thickness of 300 µm ± 10%. The compression molding was performed at 180 °C in order to crosslink the polyethylene materials. The plaques were then degassed at 70 °C for 24 hours to remove peroxide decomposition products and to ensure that all samples were in the same state.

Secondly, from the degassed 26 cm-plaques, the semiconductive electrode samples were extracted using a hole punch. The diameter of the electrodes were 24 mm. Since the compression molded 26 cm-plaques did not have uniform thickness, each of the electrode samples were measured using a micrometer such that they had a thickness of 300 µm ± 10%. Additionally, from the degassed 26 cm-insulation plaques, samples with a diameter of 50 mm were stamped out using a hole punch. Similar to the semiconductive electrode samples, only samples with a thickness of 300 µm ± 10% were saved and later used for measurements. Samples with thickness that was not within this range were discarded.

3.1.2 Metallization of the Electrodes

Plaques of insulation and semiconductive materials were prepared in the same way as described in Section 3.1.1 above. One side of the insulation plaque were fully metallized in order to form the ground electrode. High voltage electrodes with a diameter of 20 mm were sputtered on the other side of the plaque. The metallization was done using magnetron PVD, with an aluminium target.

From a single plaque, eight samples with a diameter of 50 mm was extracted using a hole punch. The metallized insulation plaque is presented in Figure 3.1.

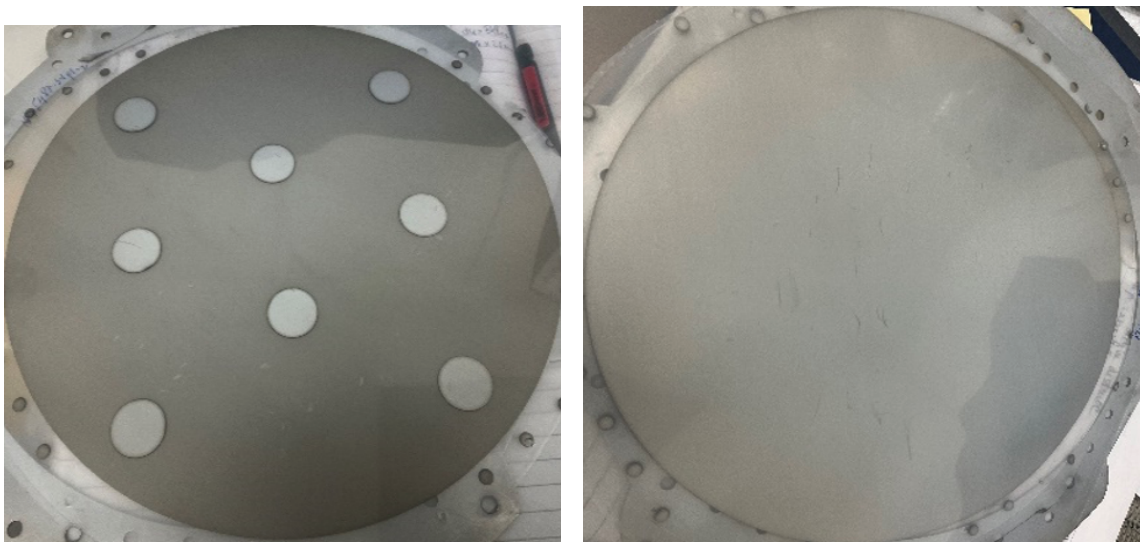

(a) Front: Eight high voltage electrodes with diameters of 20 mm sputtered onto the insulation plaque.

(b) Back: Metallization covering entire plauqe, which where the ground electrodes.

Figure 3.1: Both sides of the metallized insulation plaque.

For the metallized semiconductive electrodes, only one side of the degassed 26 mm plaque were metallized using the same sputtering method mentioned above. Metallized semiconductive electrodes were then extracted from the plaques using a hole punch. In electrode configurations 2 and 4 described in Section 3.3, high voltage electrodes with a diameter of 24 mm were used. In addition, a metallized semiconductive ground electrode with a diameter of 50 mm was used in electrode configuration 4. The metallized semiconductive plaque is presented in Figure 3.2.

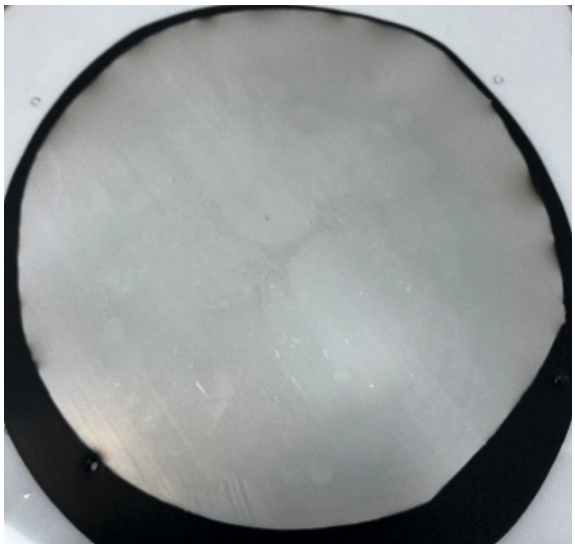

Figure 3.2: The metallized side of the semiconductive plaque.

3.2 Space Charge Measurement Procedure

All of the space charge measurements presented in this thesis were conducted in the electrical testing laboratory at Borouge International Innovation Centre in Stenungsund, using a PEA system provided by Box Elder Innovations Inc. The space charge test sequence was as follows for all measurements:

1. High voltage on for 120 minutes
2. High voltage off for 60 minutes

When the high voltage was turned on, data was recorded every 3rd second for the first minute and then once every minute for the remaining 119 minutes. Similarly, when the high voltage was turned off, data was recorded every 3rd second for the first minute followed by once every minute for the remaining 59 minutes. The increased sampling during the first minute of voltage on and voltage off was used to increase the temporal resolution just as the DC stress is applied or removed. In doing so, any transient processes such as rapid charge injection could be captured.

3.2.1 Signal Processing

A 9 µm thick gold coated poly(vinylidene fluoride-co-trifluoroethylene) (PVDF-TrFE) piezoelectric transducer was used to detect the acoustic waves. The thickness of the transducer was chosen to be 9 µm because it enabled more high frequency signal components to be captured.

The time domain electrical signal recorded from the piezoelectric transducer during the PEA measurements were signal processed using MATLAB. The signal processing script was developed in-house at Borouge International Innovation Centre in Stenungsund Sweden.

Each measurement sequence was calibrated using the initial measurement of the raw signal, such as the one presented in Figure 3.3. This calibration approach minimized potential systematic errors associated with changes in the test setup that would otherwise propagate through subsequent measurement sequences if all sequences were calibrated using the same raw signal response.

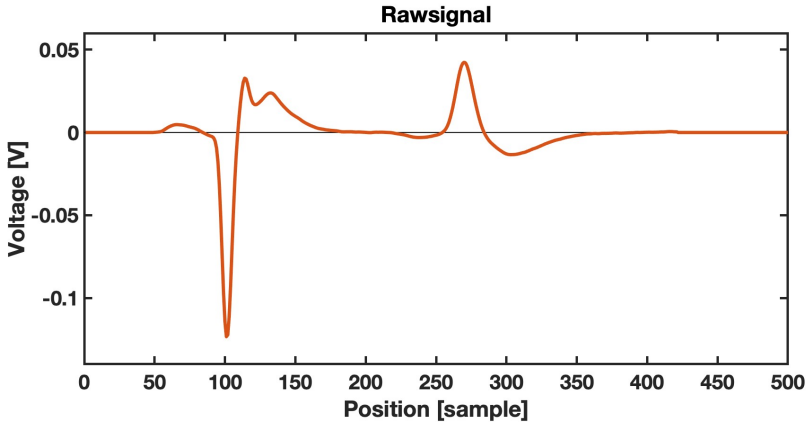

Figure 3.3: Raw signal used as calibration for PEA measurement.

The deconvolution of the recorded time domain signal was based on the Wiener deconvolution scheme. Moreover, the deconvolved space charge distributions were smoothened using a Gaussian filter. The deconconvoluted signal was tuned using the standard deviation of the Gaussian filter such that the ratio of the FWHM charge density peak of the ground electrode (d_{GND} in Figure 3.4) and the distance between the high voltage and ground peaks (d in Figure 3.4) were within 4 - 10%. This ultimately ensured that the resolution of the signal processed space charge profiles were traceable to the physical thickness of the sample [22].

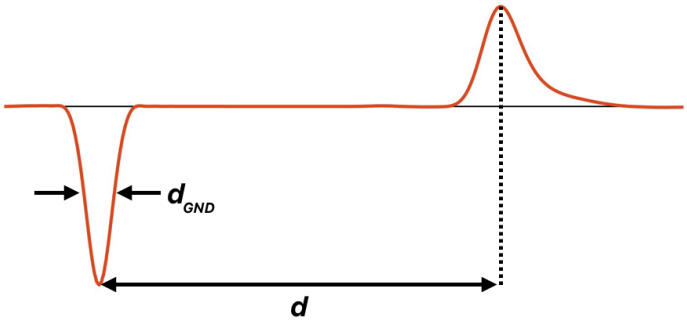

Figure 3.4: Illustration depicting how the Gaussian filter was applied to achieve a resolution that was traceable to the physical thickness of the sample.

3.3 Electrode Configurations

The four electrode configurations used in this thesis are illustrated in Figure 3.5, and the measurement sequence for electrode configurations 1, 2, 3 and 4 are presented in Tables 3.1 and 3.2. These test conditions were decided in order to gauge how the electric field and temperature influences the observed space charge accumulation obtained from the PEA measurements.

The electrode configurations were chosen such that the influence of the semiconductive electrode material and/or the influence of the ground electrode could be eliminated in a controlled and stringent manner. In turn, this electrode methodology is believed to effectively measure and/or decern whether the space charge stems from intrinsic properties of the insulation material itself, or if it is due to extrinsic processes such as charge injection from the semiconductive electrode material used in the PEA measurement setup used by Borouge International Innovation Centre in Stenungsund.

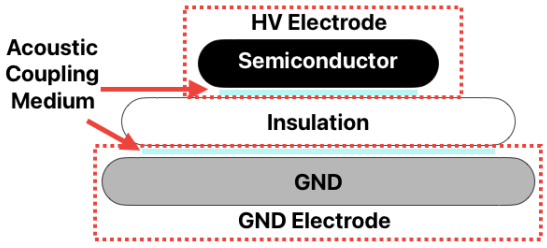

(a) Schematic illustration of electrode configuration 1.

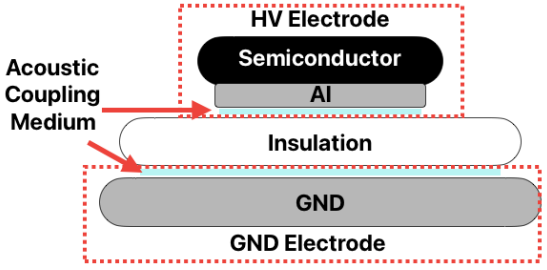

(b) Schematic illustration of electrode configuration 2.

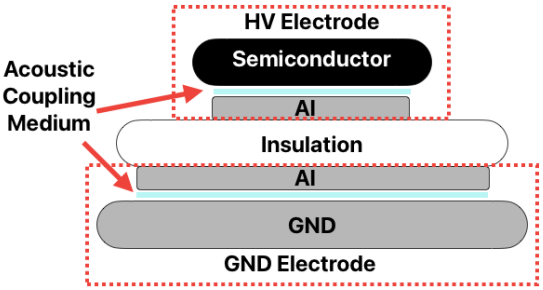

(c) Schematic illustration of electrode configuration 3.

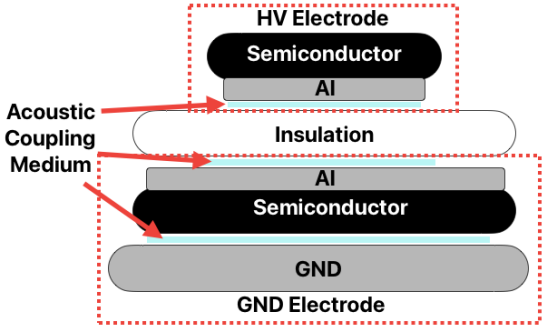

(d) Schematic illustration of electrode configuration 4.

Figure 3.5: Schematic illustrations of the four electrode configurations used in this work.

Initially, measurements were only going to be carried out using electrode configurations 1, 2, and 3. However, from the results obtained from the measurements using configurations 1-3, a fourth additional electrode configuration was also included and conducted using an applied electric field strength of 40 kV/mm at 25 °C and 70 °C. The full measurement procedure for configuration 4 is given in Table 3.2. Lastly, all four electrode configurations are illustrated in Figures 3.5a-3.5d below.

Table 3.1: Measurement procedures for electrode configuration 1, 2 and 3.

Field Strength [kV/mm]	**Temperature** [°C]	**Number of measurements**
20	25	2
20	70	2
40	25	2
40	70	2

Table 3.2: Measurement procedures for electrode configuration 4.

Field Strength [kV/mm]	**Temperature** [°C]	**Number of measurements**
40	25	2
40	70	2

3.4 Pre-screening Mesurements of Acoustic Coupling Media

The three oils that were used in this work were selected through a set of pre-screening measurements which are presented in Appendix B and outlined in Table 3.3 below. A part from oil A, four oils were pre-screened, of which three were based on the same chemical composition as oil A but in three different viscosities. The fourth and fifth oils that were pre-screened were of chemical composition 1 and 2, and different from each other and the chemical composition of oils A, B and C.

Table 3.3: Table outlining the acoustic coupling media that were pre-screened.

	Same Chemical Composition			**Composition 1**	**Composition 2**
Name	Oil A	Oil B	Oil C	Oil D	Oil E
Viscosity	Low	Medium	High	-	-

The pre-screening tests were performed at 25 °C using an electric field strength of 40 kV/mm, where the DC stress was applied for 30 minutes. From the pre-screening results of the three oils A-C of the same chemical composition, it was decided that tests were going to be carried out using oil A and C, since they exhibited the biggest difference with respect to accumulated charge. Additionally, the machine oil (oil D in Table 3.3) was excluded because it performed worst overall in terms of charge accumulation among the five oils outlined in Table 3.3.

3.5 Acoustic Coupling Media

Three different acoustic coupling media, which are outlined in Table 3.4, were tested in order to evaluate their influence on both the acoustic signal and the space charge accumulation within the XLPE insulation material. Two of the acoustic coupling media were oils of the chemical composition (oils A and C), but with different viscosities. The third oil (oil E) was a type of oil with chemical composition 2. The three oils were not only chosen due to their dielectric and chemical properties, but also through a pre-screening process outlined in the section above.

Table 3.4: Table outlining the acoustic coupling media used in this work.

	Same Chemical Composition		**Composition 2**
Name	Oil A	Oil C	Oil E
Viscosity	Low	High	-

All three coupling media were first tested using electrode configuration 1 (Figure 3.5a in Section 3.3). The measurement procedure for the coupling media is outlined in Table 3.5 below. In addition, the two oils A and C were also tested using electrode configuration 2 (Figure 3.5b in Section 3.3) according to the same measurement procedure outlined in Table 3.5. Due to the results obtained using oil E during the PEA measurements with electrode configuration 1, this oil was ultimately excluded from the subsequent measurements using electrode configuration 2. This is further discussed in Section 4.2 below.

Table 3.5: The measurement procedures for the acoustic coupling media.

Field Strength [kV/mm]	**Temperature** [°C]	**Number of measurements**
40	25	2
40	70	2

4
Results and Discussion

In the following sections the results from the conducted PEA measurements are presented and discussed. In Section 4.1, the results from the four different electrode configurations outlined in Section 3.3 are presented. For electrode configuration 1, 2 and 3, a total of eight measurements were performed, respectively. These measurements were performed using two different electric field strength and at two different temperatures, as presented in Table 3.1 in Section 3.3. In addition, four measurements were also performed using a fourth electrode configuration described in Section 3.3. The measurements carried out using the fourth electrode configuration was performed using only one electric field strength at two temperatures, given in Table 3.2 in Section 3.3. For transparency, all of the measurements from the different electrode configurations (21 measurements) as well as for the acoustic coupling agents (10 measurements) are presented in Appendix C.

4.1 Effect of Electrode Configuration on Space Charge Characteristics

The space charge characteristics near the high voltage electrode for electrode configurations 2, 3 and 4 were observed to be very similar to those of electrode configuration 1, as can be seen in Figure 4.1. In addition, this behavior was also observed in the field enhancement factors in Figure 4.2. Specifically, little to no deviation from the Laplacian field was observed at the high voltage electrode for configurations 2, 3, and 4. In contrast, electrode configuration 1 showed a decrease of roughly 10% from the Laplacian field at the high voltage electrode, thus indicating that there was an accumulation of homocharge in the vicinity of the high voltage electrode.

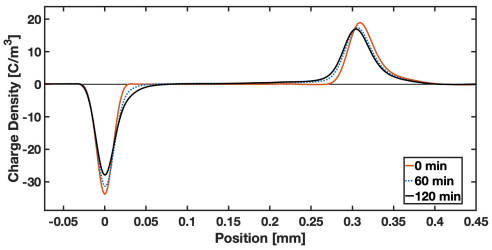

(a) Space charge profile for electrode configuration 1 using oil A at 25 °C subjected to 40 kV/mm.

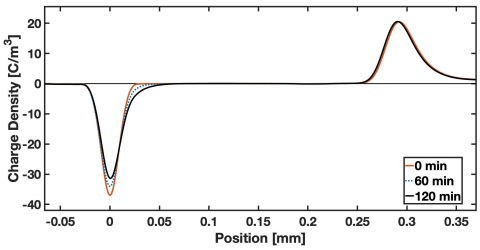

(b) Space charge profile for electrode configuration 2 using oil A at 25 °C subjected to 40 kV/mm.

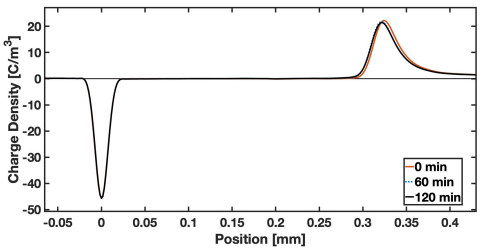

(c) Space charge profile for electrode configuration 3 using oil A at 25 °C subjected to 40 kV/mm.

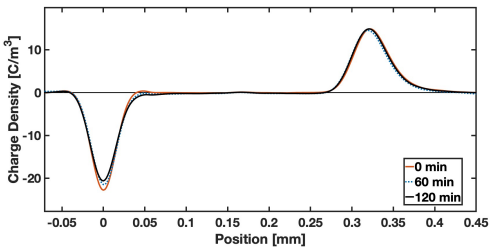

(d) Space charge profile for electrode configuration 4 using oil A at 25 °C subjected to 40 kV/mm.

Figure 4.1: Space charge profiles at 60 minute intervals during the two hours of voltage on. The measurements were performed at 25 °C with an applied electric field strength of 40 kV/mm.

The similarities in the space charge profiles near the high voltage electrodes observed in configurations 2, 3 and 4 may, in part, be linked to the surface roughness of the high voltage electrodes. According to [16], charge injection, and subsequently charge accumulation, decrease as the surface roughness decreases. Since the surface of the high voltage electrodes of configurations 2, 3 and 4 in contact with the XLPE insulation sample consisted of metallized aluminium, it can be argued that the surface roughness is much less than that of the semicon-insulation interface in

electrode configuration 1.

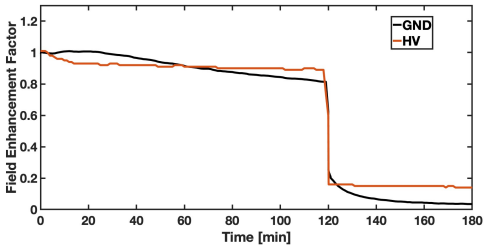

(a) Field enhancement factors of electrode configuration 1 using oil A at 25 °C subjected to 40 kV/mm.

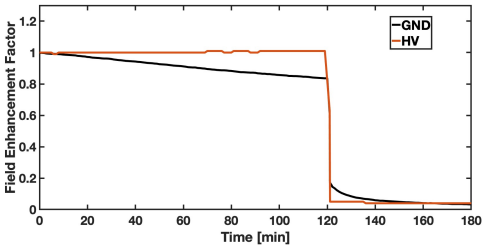

(b) Field enhancement factors of electrode configuration 2 using oil A at 25 °C subjected to 40 kV/mm.

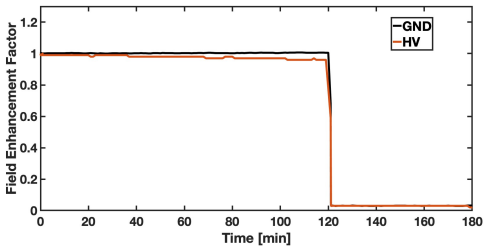

(c) Field enhancement factors of electrode configuration 3 using oil A at 25 °C subjected to 40 kV/mm.

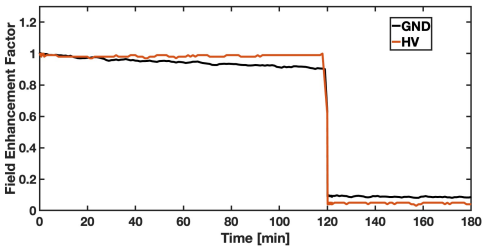

(d) Field enhancement factors of electrode configuration 4 using oil A at 25 °C subjected to 40 kV/mm.

Figure 4.2: Field enhancement factors over the duration of one full measurement cycle consisting of two hours of high voltage on followed by one hour of high voltage off. The measurements were performed at 25 °C with an applied electric field strength of 40 kV/mm.

Additionally, the space charge profiles from electrode configurations 2, 3 and 4 also indicate that the influence of the semiconductive XLPE high voltage electrode can be greatly reduced. By comparing the space charge profiles in Figure 4.1, the charge accumulation characteristics near the high voltage electrode for configurations 2, 3 and 4 were very consistent. This indicates that the placement of the metallized layer has little effect on the overall space charge profile. That is, the same charge injection behavior from the high voltage electrode was observed independently of whether the metallization layer was adhered to the semiconductive XLPE electrode or to the XLPE insulation sample. Most notably, the inhibition of charge injection due to the metallization of the high voltage electrode was observed in the field enhancement factors in Figure 4.2b, 4.2c and 4.2d.

The behavior at the high voltage electrode was thus very consistent across the configurations with metallized high voltage electrodes. Comparing the charge injection at the ground electrode between electrode configurations 1–4 in Figure 4.1, a substantial reduction in charge injection was observed for configurations 3 and 4 utilizing a metallized ground electrode. When the ground electrode was sputtered

directly onto the insulation sample, as in electrode configuration 3, no charge accumulation or charge injection was observed near the ground electrode. In contrast, when a metallized semicon electrode was used as a ground electrode, some charge accumulation at the ground electrode was observed.

It can be argued that the ground-insulation interface is optimized in electrode configuration 3. Optimized in the sense that when the ground electrode is sputtered directly onto the sample, it fills out most of the surface roughness of the XLPE insulation sample, hence facilitating an optimum ground electrode which inhibits charge injection, as can be seen in Figure 4.1c.

The observed space charge profiles obtained when both electrodes were metallized showed no charge injection from the electrodes into the XLPE sample. Consistent for both electrode configurations 3 and 4 was that their space charge profiles mostly showed surface charges at the electrode-sample interfaces. As is indicated by the space charge profiles in Figure 4.1c and 4.1d, the main differences were the behavior of the ground electrodes.

This is believed to be due to the decreased effective surface roughness of the ground electrode in configuration 3, decreasing the overall charge injection from the ground electrode. In addition, when the ground electrode is directly sputtered onto the XLPE sample, the metallization will also decouple the influence of the acoustic coupling medium from the XLPE sample itself. In configuration 4, there is no such decoupling taking place between the ground electrode and the XLPE sample. Therefore, the increased surface charge accumulation at the ground electrode observed in the space charge profile for configuration 4 is believed to be due to the interaction between the coupling medium and the XLPE insulation sample.

What is more, the total acoustic path length of electrode configuration 4 was increased due to the added metallized semiconductive XLPE ground electrode. Compared to configurations 1, 2 and 3, the acoustic waves had to propagate through more material, leading to significant dampening of the acoustic waves. When comparing the amplitudes of the electrode peaks between configurations 1–4 in Figure 4.1, the ground electrode peak in configuration 4 was about 33% weaker than the ground electrode peak observed in configuration 1 and approximately 30% weaker than the ground electrode peaks in configurations 2 and 3. In addition, the added material in configuration 4 also contributed to more dispersive effects compared to configurations 1–3, which was observed as a loss of high-frequency wave contributions, leading to an overall broadening of the electrode peaks.

4.1.1 Electric Field Dependence

The space charge profiles and the field enhancement factors for electrode configurations 1, 2 and 3 at an applied electric field strength of 20 kV/mm performed at 25 °C are presented in Figure 4.3. The applied electric field strength used during the measurements was shown to have no impact on the space charge characteristics of electrode configurations 2 and 3. However, a noticeable electric field dependence on the charge injection from the high voltage electrode was observed for electrode configuration 1.

From the space charge profile of configuration 1 in Figure 4.3a, almost no charge injection was observed from the high voltage electrode at an applied electric field strength of 20 kV/mm. Comparing the field enhancement factors near the high voltage electrode in Figures 4.3b and 4.2a at 20 kV/mm and 40 kV/mm, there was notably more accumulation of homocharge at 40 kV/mm. At 20 kV/mm, the local electric field near the high voltage electrode was highly stable with no significant deviation from the Laplacian field.

Similar electric field dependence was observed at the ground electrode as well. As can be seen in Figures 4.3a and 4.1a, there was more accumulation of homocharge near the ground electrode at 40 kV/mm compared to at 20 kV/mm. This suggests that the observed charge injection from the electrodes in configuration 1 was primarily field assisted.

As stated above, the space charge characteristics of electrode configuration 2 were not noticeably impacted by the applied DC stress. Surprisingly, at 20 kV/mm there was noticeably more homocharge accumulation at the ground electrode for configuration 2 compared to configuration 1, as can be seen in the field enhancement factors in Figures 4.3d and 4.2b, respectively. Even though both configurations 1 and 2 effectively had the same ground electrodes, more charge injection was observed at the ground electrode of configuration 2. In addition, the charge accumulation at the ground electrode observed for configuration 2 was not observed to be noticeably affected by the DC stress. This may suggest that a more complex interfacial phenomenon is taking place that cannot be explained by the applied electric field alone.

This behavior is in part believed to be attributed to the altered band structure of the semicon-metallization-insulation interface at the high voltage electrode, forming a higher Schottky barrier. As a result, far fewer charge carriers are being injected and emitted through the high voltage electrode. Hence forcing charge to accumulate near the ground electrode in order to satisfy Poisson's equation throughout the insulation sample. Additionally, the surface roughness of the metallized high voltage electrode in configuration 2 may also inhibit the injection and emission of charge carriers.

For electrode configuration 3 there was no observable difference between the space charge profiles presented in Figures 4.3e and 4.1c subjected to 20 kV/mm and 40 kV/mm, respectively. Moreover, due to the metallization on both sides of the insulation sample, the ground electrode will behave in a similar way as the high voltage electrode in configuration 2 with regards to injection and emission of charge carriers. What is more, due to there being a metallized aluminium layer inhibiting the acoustic coupling media to be in direct contact with the XLPE sample. Thus both the effects of the semiconductive electrode material and the acoustic coupling medium are decoupled from the XLPE insulation sample itself. Therefore, it is believed that what is observed in the space charge profiles in both Figures 4.3e and 4.1c is the intrinsic space charge dynamics of the XLPE insulation sample subjected to 20 kV/mm and 40 kV/mm, respectively.

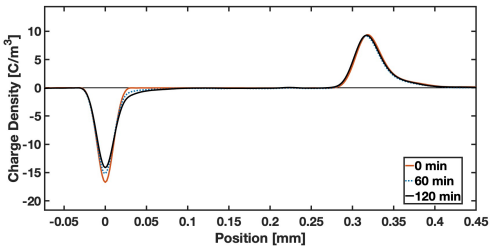

(a) Space charge profile for electrode configuration 1 using oil A at 25 °C subjected to 20 kV/mm.

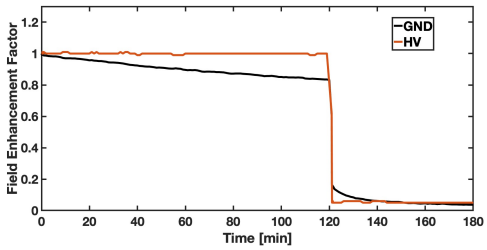

(b) Field enhancement factors of electrode configuration 1 using oil A at 25 °C subjected to 20 kV/mm.

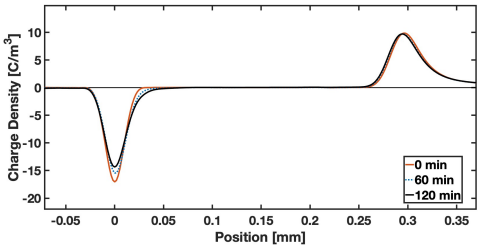

(c) Space charge profile for electrode configuration 2 using oil A at 25 °C subjected to 20 kV/mm.

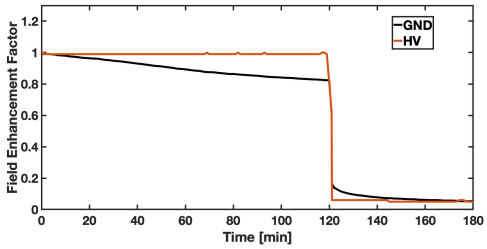

(d) Field enhancement factors of electrode configuration 2 using oil A at 25 °C subjected to 20 kV/mm.

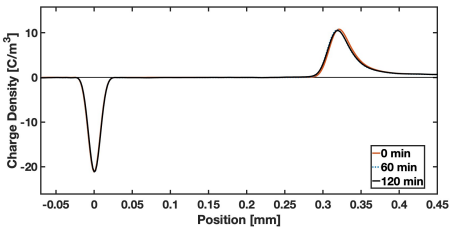

(e) Space charge profile for electrode configuration 3 using oil A at 25 °C subjected to 20 kV/mm.

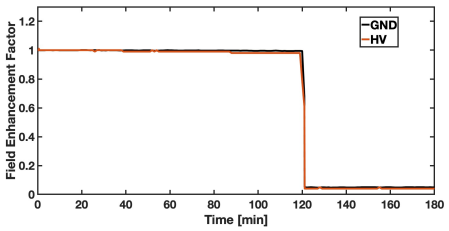

(f) Field enhancement factors of electrode configuration 3 using oil A at 25 °C subjected to 20 kV/mm.

Figure 4.3: Space charge profiles at 60 minute intervals during the two hours of voltage on, with their corresponding field enhancement factors. The measurements were performed at 25 °C with an applied electric field strength of 20 kV/mm.

4.1.2 Temperature Dependence

The space charge profiles and the field enhancement factors from the PEA measurements performed at 70 °C with an applied electric field strength of 40 kV/mm are presented in Figure 4.4 and 4.5, respectively. In addition, the space charge profiles and field enhancement factors from the PEA measurements using electrode configurations 1, 2 and 3 performed at 70 °C with an applied field strength of 20 kV/mm are given in Figure 4.6.

Electrode configuration 1 showed a decrease in the penetration depth of the accumulated charge near the ground electrode at 70 °C compared to at 25 °C. As can be seen in Figures 4.1a and 4.4a, the charge accumulation was also observed to be more concentrated at the electrode-sample interface at 70 °C. This is believed to be due to the increased charge carrier mobility, which increases the trapping and de-trapping rates within the XLPE sample material, causing more homocharge to accumulate at the electrode-sample interface.

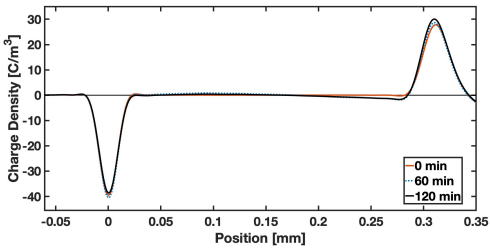

(a) Space charge profile for electrode configuration 1 using oil A at 70 °C subjected to 40 kV/mm.

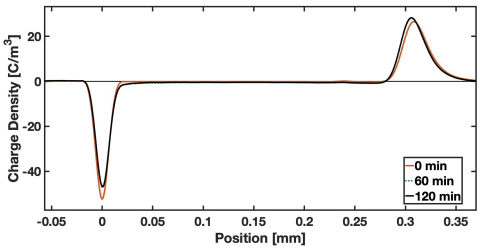

(b) Space charge profile for electrode configuration 2 using oil A at 70 °C subjected to 40 kV/mm.

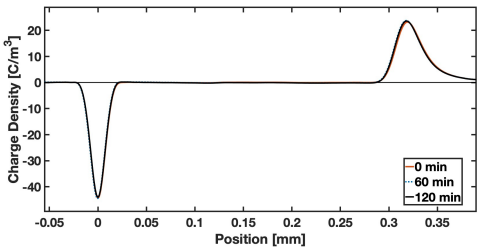

(c) Space charge profile for electrode configuration 3 using oil A at 70 °C subjected to 40 kV/mm.

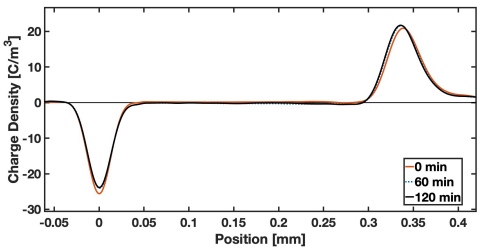

(d) Space charge profile for electrode configuration 4 using oil A at 70 °C subjected to 40 kV/mm.

Figure 4.4: Space charge profiles at 60 minute intervals during the two hours of voltage on, with their corresponding field enhancement factors. The measurements were performed at 70 °C with an applied electric field strength of 40 kV/mm.

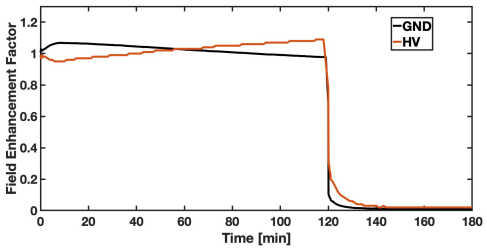

(a) Field enhancement factors of electrode configuration 4 using oil A at 70 °C subjected to 40 kV/mm.

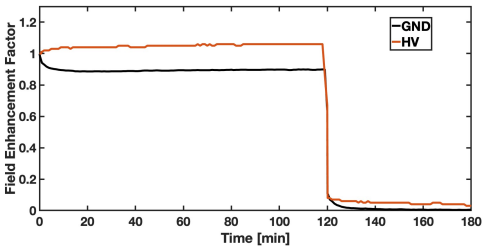

(b) Field enhancement factors of electrode configuration 2 using oil A at 70 °C subjected to 40 kV/mm.

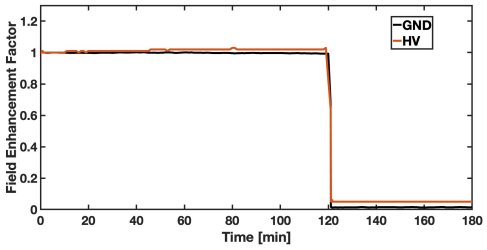

(c) Field enhancement factors of electrode configuration 3 using oil A at 70 °C subjected to 40 kV/mm.

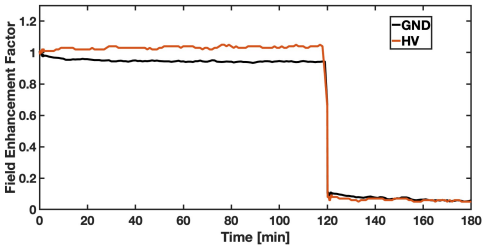

(d) Field enhancement factors of electrode configuration 4 using oil A at 70 °C subjected to 40 kV/mm.

Figure 4.5: Field enhancement factors over the duration of one full measurement cycle consisting of two hours of high voltage on followed by one hour of high voltage off. The measurements were performed at 70 °C with an applied electric field strength of 40 kV/mm.

Configuration 2 and 4 were observed to have a similar type of temperature dependence when it came to local electric field variations at the electrodes. As can be seen in the field enhancement factors at the ground electrodes in Figures 4.2b, 4.2d, 4.5b and 4.5d, both configurations exhibited slow decay at 20 °C, reaching roughly 20% and 10% below the Laplacian field after 2 hours of voltage on. At 70 °C, both field enhancement factors exhibited a faster decay, reaching a stable steady state of 20% and 10% below the Laplacian field after 2 hours of voltage on. This was consistent with higher charge carrier mobility and increased Schottky injection expected at higher temperatures.

Moreover, it is believed that the difference between the decay times and steady state values of the field enhancement factors at the ground electrodes of configuration 2 and 4 stems from the difference in surface roughness exhibited by the two ground electrodes. Consistent with the literature, charge accumulation is observed to increase with increased surface roughness, as can be seen in Figures 4.4b and 4.4d.

At 70 °C, the field enhancement factors were observed to consistently increase above the Laplacian field at the high voltage electrodes in configurations 1, 2 and 4, indicative of heterocharge accumulation. In addition, the space charge profiles presented in Figures 4.1c and 4.4c for electrode configuration 3 showed no noticeable difference when the temperature was increased. As mentioned in the previous section, both the acoustic coupling medium and the semiconductive electrode material were decoupled from the XLPE insulation sample as a result of the metallization of the sample.

It is therefore believed that the field enhancement near the high voltage electrode at 70 °C is in part caused by migration of the acoustic coupling medium into the XLPE insulation sample, resulting in heterocharge accumulation. As the temperature increases, the conductivity and permittivity of the coupling medium and the XLPE sample change at different rates, resulting in a greater mismatch. This may further enhance Maxwell-Wagner polarization at the oil-sample interface, which is believed to be the main contributor driving the field enhancement at the high voltage electrode in configuration 1 seen in Figure 4.5a.

Consistent in the space charge profiles for all configurations was that the amplitude of the peaks for the high voltage and ground electrodes was higher at 70 °C. This can be attributed to the thermal expansion of the XLPE materials of the insulation sample and semiconductive electrodes, resulting in less reflection of the acoustic waves.

As can be seen in Figure 4.6 below, the space charge dynamics of electrode configuration 2 and 3 were observed to behave in a similar way when subjected to a DC stress of 20 kV/mm. Interestingly, the heterocharge accumulation seems to be exacerbated at the high voltage electrode for configuration 1 at 20 kV/mm.

The main reason for the increased field enhancement near the high voltage electrode in configuration 1 is believed to stem from the fact that the charge injection is lower at 20 kV/mm. Thus, the charge accumulation near the electrode is not driven by the rapid charge injection from the high voltage electrode observed at 40 kV/mm, but is instead dominated by the interfacial permittivity/conductivity mismatch between the acoustic coupling medium and the XLPE insulation material.

Moreover, audible crackling sounds were observed when the PEA measurements were conducted using electrode configuration 4 at 70 °C. This is believed to stem from partial discharges happening at the sample-oil-electrode interface. Initially, the PEA measurements using configuration 4 were performed using a ground electrode that was 34 mm in diameter. However, at 70 °C the ground electrode was observed to have physically shifted laterally of center from where it was placed initially. The physical lateral shift of the ground electrode was observed to cause a drop in the local fields at both electrodes.

The cause of the lateral force exerted onto the ground electrode is unknown. In addition, all measurements presented above using electrode configuration 4 were performed using a ground electrode with a diameter of 50 mm, as is outlined in Section 3.3. Due to the system instability observed at 70 °C, only one measurement for configuration 4 at 70 °C could be properly deconvolved without artifacts.

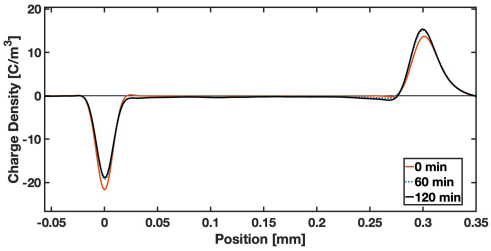

(a) Space charge profile for electrode configuration 1 using oil A at 70 °C subjected to 20 kV/mm.

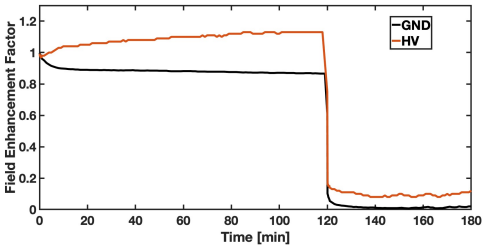

(b) Field enhancement factors of electrode configuration 1 using oil A at 70 °C subjected to 20 kV/mm.

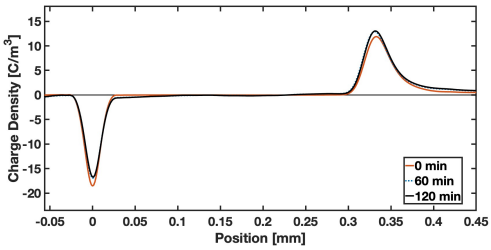

(c) Space charge profile for electrode configuration 2 using oil A at 70 °C subjected to 20 kV/mm.

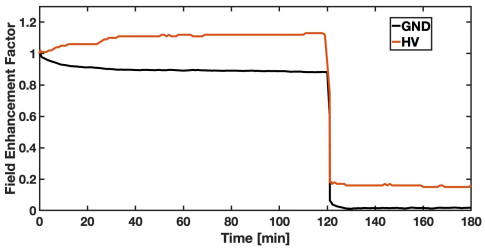

(d) Field enhancement factors of electrode configuration 2 using oil A at 70 °C subjected to 20 kV/mm.

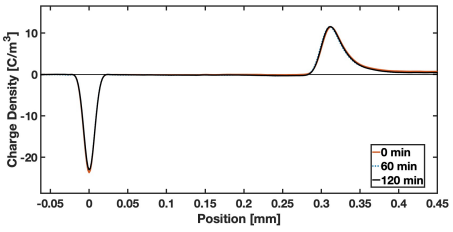

(e) Space charge profile for electrode configuration 3 using oil A at 70 °C subjected to 20 kV/mm.

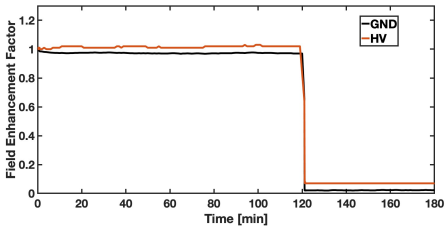

(f) Field enhancement factors of electrode configuration 3 using oil A at 70 °C subjected to 20 kV/mm.

Figure 4.6: Space charge profiles at 60 minute intervals during the two hours of voltage on, with their corresponding field enhancement factors. The measurements were performed at 70 °C with an applied electric field strength of 20 kV/mm.

4.2 Effect of Acoustic Coupling Medium on Space Charge Characteristics

From the space charge profiles in Figure 4.7 using electrode configuration 1, oil C showed substantially more charge injection and space charge accumulation at 25 °C compared to oil A and oil E. Comparing the field enhancement factors at the high voltage electrode in Figures 4.7b, 4.7d and 4.7f, the rapid injection of homocharge was observed for all three oils. The local electric field at the high voltage electrode was observed to reach steady-state roughly 10% below the Laplacian field after 15 minutes for both oil A and E. From the field enhancement factor at the high voltage electrode presented in Figure 4.7d using oil E, charge accumulation was observed to increase during the 2 hours of voltage on. Moreover, the continuous charge accumulation was observed to result in a reduction of roughly 20% below the Laplacian field at the high voltage electrode after 2 hours.

The space charge accumulation near the ground electrode was observed to be very similar at 25 °C for oils A and E when used as coupling agents in electrode configuration 1, as can be seen in Figures 4.7a and 4.7e. The similarities were also observed in the field enhancement factor given in Figures 4.7b and 4.7f using oil A and E, respectively. The substantial homocharge accumulation in the vicinity of the ground electrode was observed to reduce the local electric field strength at the ground electrode by roughly 30% from the Laplacian field after 2 hours of voltage on, which can be seen in Figure 4.7d.

At 70 °C, both oil A and E exhibited increasing heterocharge accumulation near the high voltage electrode, reaching approximately 5% and 20% above the Laplacian field after two hours of voltage on for oil A and E, respectively. Interestingly, the field enhancement factors for oil A presented in Figure 4.8b initially showed homocharge accumulation near the high voltage electrode and heterocharge accumulation near the ground electrode, symmetrically distributed (±5%) around the Laplacian field. After roughly 10 minutes of voltage application, both field enhancement factors crossed the Laplacian field, indicating a redistribution of space charge characterized by increasing homocharge accumulation near the ground electrode and increasing heterocharge accumulation near the high voltage electrode. After 2 hours of applied DC stress, the electric field strengths were again observed to be symmetrically distributed (±5%) around the Laplacian field.

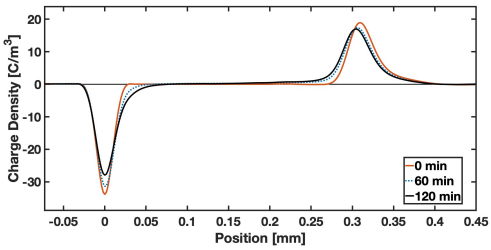

(a) Space charge profile for electrode configuration 1 using oil A at 25 °C subjected to 40 kV/mm.

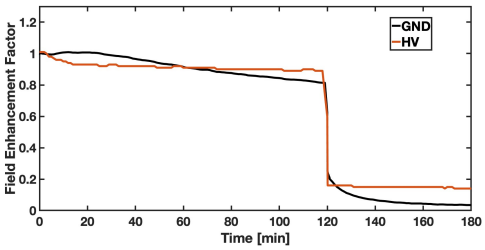

(b) Field enhancement factors of electrode configuration 1 using oil A at 25 °C subjected to 40 kV/mm.

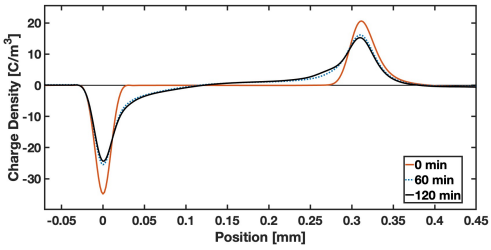

(c) Space charge profile for electrode configuration 1 using oil C at 25 °C subjected to 40 kV/mm.

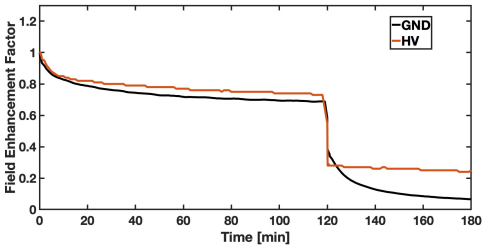

(d) Field enhancement factors of electrode configuration 1 using oil C at 25 °C subjected to 40 kV/mm.

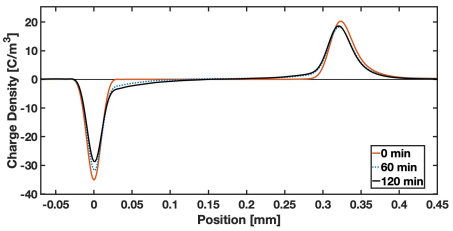

(e) Space charge profile for electrode configuration 1 using oil E at 25 °C subjected to 40 kV/mm.

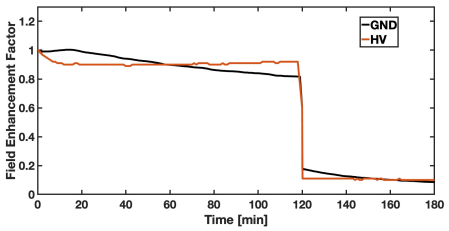

(f) Field enhancement factors of electrode configuration 1 using oil E at 25 °C subjected to 40 kV/mm.

Figure 4.7: Space charge profiles at 60 minute intervals during the two hours of voltage on, with their corresponding field enhancement factors. The measurements were performed at 25 °C with an applied electric field strength of 40 kV/mm.

Comparing the amplitudes of the electrode peaks between the space charge profiles presented in Figures 4.8a, 4.8c and 4.8e, oil E appeared to enhance the acoustic coupling. However, oil E was also observed to soften both the XLPE semicon electrode and the XLPE insulation sample materials, which likely resulted in more swelling than the expected thermal expansion of the XLPE materials. Thus, the effective mechanical pressure exerted onto the electrode-sample stack was believed to be higher when oil E was used as an acoustic coupling agent.

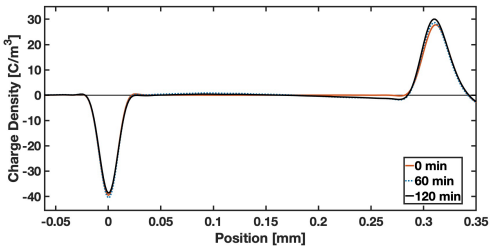

(a) Space charge profile for electrode configuration 1 using oil A at 70 °C subjected to 40 kV/mm.

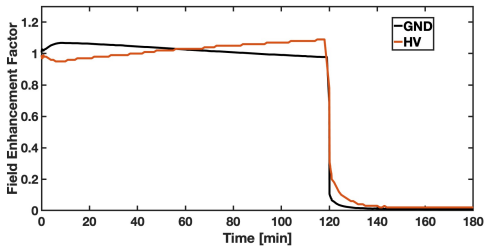

(b) Field enhancement factors of electrode configuration 1 using oil A at 70 °C subjected to 40 kV/mm.

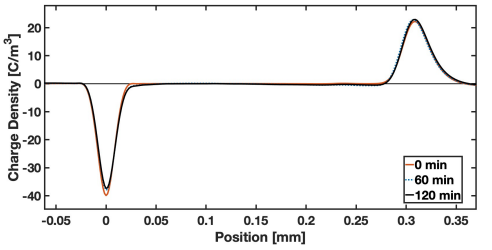

(c) Space charge profile for electrode configuration 1 using oil C at 70 °C subjected to 40 kV/mm.

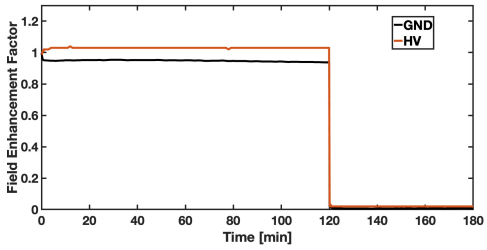

(d) Field enhancement factors of electrode configuration 1 using oil C at 70 °C subjected to 40 kV/mm.

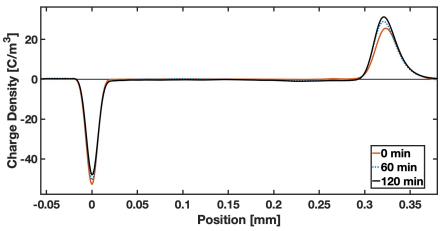

(e) Space charge profile for electrode configuration 1 using oil E at 70 °C subjected to 40 kV/mm.

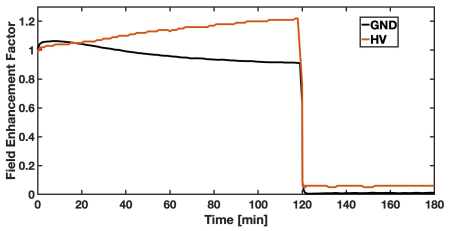

(f) Field enhancement factors of electrode configuration 1 using oil E at 70 °C subjected to 40 kV/mm.

Figure 4.8: Space charge profiles at 60 minute intervals during the two hours of voltage on, with their corresponding field enhancement factors. The measurements were performed at 70 °C with an applied electric field strength of 40 kV/mm.

As mentioned in the previous section, when decoupling the semiconductive electrode material using electrode configuration 2 outlined in Section 3.3, almost no charge injection was observed at the high voltage electrode at 25 °C when oil A was used as an acoustic coupling medium, depicted in Figure 4.9a. Additionally, no observable difference was observed in the charge injection from the ground electrode between electrode configurations 1 and 2 when oil A was used as an acoustic coupling medium.

As can be seen in Figure 4.9c, when oil C was used as an acoustic coupling medium, substantially more charge injection from the ground electrode was observed compared to when oil A was used. From Figure 4.9d, the field enhancement factor at the ground electrode was observed to decrease approximately 35% below the Laplacian field after 2 hours of an applied DC stress of 40 kV/mm. From both the space charge profile and the field enhancement factor presented in Figures 4.9c and 4.9d, heterocharge was observed to accumulate at the high voltage electrode.

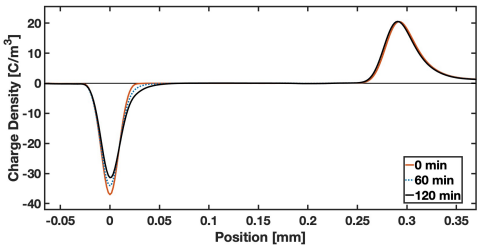

(a) Space charge profile for electrode configuration 2 using oil A at 25 °C subjected to 40 kV/mm.

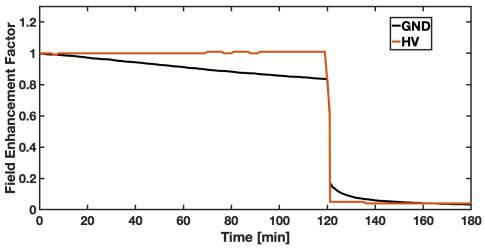

(b) Field enhancement factors of electrode configuration 2 using oil A at 25 °C subjected to 40 kV/mm.

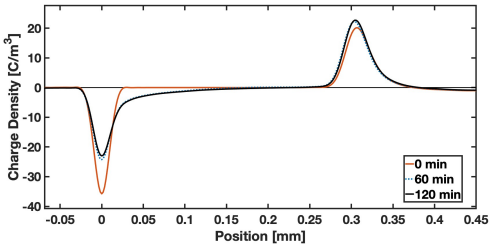

(c) Space charge profile for electrode configuration 2 using oil C at 25 °C subjected to 40 kV/mm.

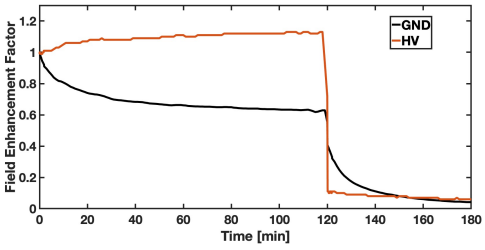

(d) Field enhancement factors of electrode configuration 2 using oil C at 25 °C subjected to 40 kV/mm.

Figure 4.9: Space charge profiles at 60 minute intervals during the two hours of voltage on, with their corresponding field enhancement factors. The measurements were performed at 25 °C with an applied electric field strength of 40 kV/mm.

At 70 °C, substantially more charge injection from the ground electrode was observed when oil C was used as a coupling agent compared to oil A. As can be seen in Figures 4.10a and 4.10c, when oil C was used, the space charge was observed to penetrate roughly twice as far into the XLPE sample compared to when oil A was used. The differences in homocharge accumulation at the ground electrodes were also observed in the field enhancement factors in Figures 4.10b and 4.10d, where the local field strength was observed to decrease approximately 10% and 20% from the Laplacian field using oil A and C, respectively.

Interestingly, the behavior of the local electric fields, and subsequently, the space charge profiles, at the high voltage electrode was observed to be very consistent for both oil A and C. As can be seen in Figures 4.10b and 4.10d, both field enhancement factors at the high voltage electrode reached steady state roughly 5% above the Laplacian field after approximately 15 minutes and 2 minutes for oil A and C, respectively.

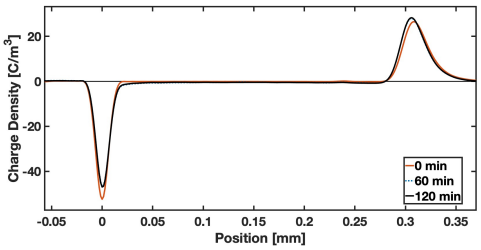

(a) Space charge profile for electrode configuration 2 using oil A at 70 °C subjected to 40 kV/mm.

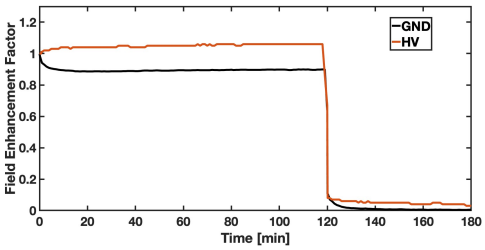

(b) Field enhancement factors of electrode configuration 2 using oil A at 70 °C subjected to 40 kV/mm.

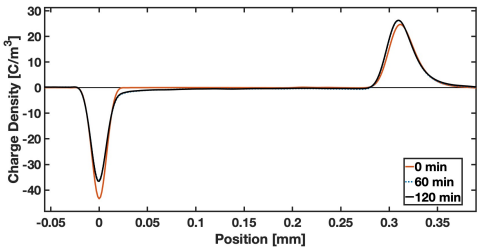

(c) Space charge profile for electrode configuration 2 using oil A at 70 °C subjected to 40 kV/mm.

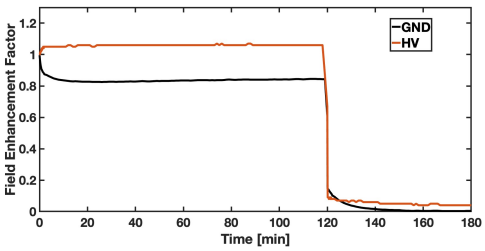

(d) Field enhancement factors of electrode configuration 2 using oil C at 70 °C subjected to 40 kV/mm.

Figure 4.10: Space charge profiles at 60 minute intervals during the two hours of voltage on, with their corresponding field enhancement factors. The measurements were performed at 70 °C with an applied electric field strength of 40 kV/mm.

From these results it is believed that oil C was forming thicker interfacial layers compared to both oils A and E, thus making it more susceptible to Maxwell-Wagner interfacial polarization resulting in more heterocharge accumulation at the high voltage electrode of the XLPE insulation sample. It is further believed that when oil C was used as a coupling medium with electrode configuration 1 at 70 °C, the conductivity mismatch between the XLPE sample and electrode materials resulted in Maxwell-Wagner interfacial polarization being the most dominant process at the high voltage electrode, thereby reducing the relative influence of direct charge injection associated with the semiconductive XLPE electrode material. Oil C was also shown to induce longer depolarization in the XLPE insulation at 25 °C compared to oil A, which can be seen in Figures 4.7d and 4.9d.

The results also showed that oil A generally performed better at 25 °C, compared to oil C and E in terms of the amount of charge injection, especially when used with electrode configuration 2. The results further indicated that oil A performed better across the temperature ranges. When used as coupling agent together with electrode configuration 1 at 70 °C, it is believed that the charge injection associated with the XLPE semicon electrode is the most dominating process initially, indicated by the rapid homocharge injection observed in Figure 4.8b. However, after approximately 15 minutes of applied DC stress, the observed transition toward heterocharge accumulation at the high voltage electrode suggests that Maxwell–Wagner polarization became increasingly dominant relative to the charge injection from the XLPE semiconductive material.

At 25 °C, the results obtained using oil E as a coupling agent initially appeared promising, as indicated by the space charge profile presented in Figure 4.8e. However, the measurements obtained at 70 °C could not clearly determine the extent to which the migration of oil E into the XLPE insulation and semiconductive materials affected the measured space charge. Significant expansion of both the semiconductive and insulating XLPE materials was observed, which is believed to have increased the effective mechanical pressure within the measurement setup. This is likely the reason why the acoustic coupling appeared to improve when oil E was used.

Based on the observed temperature dependence of the different oils with regard to the amount of charge injection, the results indicate that none of the oils are ideal to use in a temperature cycling measurement scheme. If the need for temperature cycling would arise, oil A would perform the best in terms of temperature stability and charge injection based on the results presented above.

5
Conclusions and Future Work

The goal of this thesis was to investigate how different electrode configurations and acoustic coupling agents influence the charge injection and overall space charge characteristics of the PEA measurements conducted at the electrical testing laboratory at Borouge International Innovation Centre in Stenungsund, Sweden. The main findings from the PEA measurements conducted during this work are summarized in Section 5.1. Recommended future work that may provide more insight into the results presented in this work is presented in Section 5.2.

5.1 Conclusions

5.1.1 Effect of Electrode Configuration on Space Charge Characteristics

This work has successfully demonstrated that electrode configurations with metallized high voltage electrodes (configurations 2–4) reduce the influence of the XLPE semiconductive electrode high voltage, showing little to no deviation from the Laplacian field at the high voltage electrode under the tested conditions. Thus demonstrating that metallization of the high voltage XLPE electrode material inhibits charge injection into the XLPE insulation material. In addition, results showed that the placement of the metallization layer did not significantly affect the overall charge injection behavior from the high voltage electrode.

By sputtering the ground electrode directly onto the XLPE sample (configuration 3), no charge injection from the ground electrode was observed. The effect of surface roughness of the ground electrode was also shown to impact the charge injection, where the metallized semiconductive XLPE ground electrode (configuration 4) exhibited less charge injection from the ground electrode compared to configuration 2, which both utilized the same high voltage electrode.

Electrode configuration 1 showed clear electric field dependence, with increased charge accumulation at higher DC stress, while configurations 2 and 3 showed little to no dependence on the applied DC stress. Configuration 3 showed no observable difference between measurements at 20 kV/mm and 40 kV/mm.

At 70 °C, increased charge carrier mobility resulted in more concentrated charge accumulation near the electrode-sample interfaces. Heterocharge accumulation at the high voltage electrode was observed for configurations 1, 2 and 4, while configuration 3 showed no noticeable change with temperature.

Lastly, this work has demonstrated that metallized electrodes reduce charge injection into the XLPE insulation sample. The results further indicated that by sputtering the electrodes directly onto the XLPE insulation sample, the effects of the acoustic coupling medium and the semiconductive electrode material were decoupled from the XLPE sample. Thus enabling the measurement of the space charge dynamics intrinsic to the XLPE insulation material itself.

5.1.2 Effect of Acoustic Coupling Medium on Space Charge Characteristics

The results of this work demonstrated that both the choice of acoustic coupling medium and electrode configuration significantly influence the space charge behavior and charge injection into the XLPE insulation sample under DC stress.

At 25 °C, oil C resulted in substantially higher charge injection and space charge accumulation compared to oils A and E, while oil A consistently showed the lowest injection levels, particularly when combined with electrode configuration 2. At 70 °C, a transition from homocharge injection to heterocharge accumulation was observed for oils A and E, indicating an increasing influence of Maxwell-Wagner interfacial polarization over time. Oil C was shown to induce more heterocharge accumulation at the high voltage electrode, suggesting that its higher viscosity formed a thicker oil layer, thus enhancing the effects of Maxwell–Wagner interfacial polarization compared to oil A.

Oil E appeared to improve the acoustic coupling. However, at 70 °C it was observed to migrate fully into the XLPE sample (and semicon electrode), causing increased material swelling that is believed to have resulted in an increase in the effective mechanical pressure exerted onto the sample. Thus reducing the reliability of the results obtained using oil E as an acoustic coupling medium.

Overall, oil A provided the most stable and consistent behavior across both temperature ranges and configurations, whereas oil C enhanced Maxwell-Wagner interfacial polarization effects leading to increased heterocharge accumulation. Oil E migrated into both the XLPE sample and semicon electrode materials at 70 °C, and should therefore not be used as an acoustic coupling medium.

5.2 Future Work

5.2.1 Acoustic Impedance of Coupling Medium

Previous work has been done to measure the speed of sound in oils of the same chemical composition as oil A and C. However, these studies did not take the viscosity of the oil into account. Therefore, it would be interesting to investigate to what extent the speed of sound varies with viscosity for oils with the same chemical composition. This would in turn make it possible to numerically evaluate the acoustic mismatch between potential coupling agents and dielectric samples, and therefore also the reflection coefficient.

5.2.2 Measure The Conductivity of The Acoustic Coupling Medium

The results presented in this thesis indicates that interfacial polarization at the oil-sample interface contributes to heterocharge accumulation at the high voltage electrode, especially at elevated temperatures. It would therefore be insightful to measure the conductivity of the coupling medium at different temperature ranges. A part from the field enhancement used in this work, it would provide a more quantitative insight into how the interfacial polarization affects the PEA measurements.

5.2.3 Investigate Coupling Media With Lower Viscosity

From the results of this work, charge injection was observed to increase with viscosity at 25 °C under a DC stress of 40 kV/mm. It would be interesting to investigate whether an acoustic coupling agent, preferably with the same chemical composition as oil A and C, with lower viscosity would contribute less with respect to charge injection into the sample. Additionally, it would also be interesting to investigate whether an acoustic coupling agent with lower viscosity is more stable than oil A across the temperature range used in this work.

Bibliography

[1] M. Ardelean and P. Minnebo, "HVDC Submarine Power Cables in the World: State-of-the-Art Knowledge," *JRC Publications Repository*, 2015. DOI: 10.2790/957356.

[2] G. Mazzanti and M. Marzinotto, *Extruded Cables for High-Voltage Direct-Current Transmission: Advances in Research and Development*. John Wiley & Sons, Hoboken, New Jersey, 2013, ISBN: 9781118590423.

[3] M. P. Bahrman and B. K. Johnson, "The ABCs of HVDC transmission technologies," *IEEE Power and Energy Magazine*, vol. 5, no. 2, pp. 32–44, Mar. 2007, ISSN: 1558-4216. DOI: 10.1109/MPAE.2007.329194. Accessed: Mar. 19, 2026. [Online]. Available: https://ieeexplore.ieee.org/document/4126468/.

[4] T. Hanley, R. Burford, R. Fleming, and K. Barber, "A general review of polymeric insulation for use in HVDC cables," *IEEE Electrical Insulation Magazine*, vol. 19, no. 1, pp. 13–24, Jan. 2003, ISSN: 1558-4402. DOI: 10.1109/MEI.2003.1178104. Accessed: May 19, 2026. [Online]. Available: https://ieeexplore.ieee.org/document/1178104.

[5] R. Hampton, "Some of the considerations for materials operating under high-voltage, direct- current stresses," *IEEE Electrical Insulation Magazine*, vol. 24, no. 1, pp. 5–13, Jan. 2008, ISSN: 1558-4402. DOI: 10.1109/MEI.2008.4455498. Accessed: May 19, 2026. [Online]. Available: https://ieeexplore.ieee.org/document/4455498/.

[6] M. Salah Khalil, "International research and development trends and problems of HVDC cables with polymeric insulation," *IEEE Electrical Insulation Magazine*, vol. 13, no. 6, pp. 35–47, Nov. 1997, ISSN: 1558-4402. DOI: 10.1109/57.637152. Accessed: May 19, 2026. [Online]. Available: https://ieeexplore.ieee.org/document/637152/.

[7] L. Dissado and J. Fothergil, *Electrical Degradation and Breakdown in Polymers*. The Institution of Engineering and Technology, London, 1992, ISBN: 978-0-86341-196-0.

[8] T. Takada, H. Ren, J. Li, W. Wang, X. Chen, and Q. Li, *Electric Charge Accumulation in Dielectrics: Measurement and Analysis*, en. Singapore: Springer Nature, Singapore, 2022, ISBN: 978-981-19-6155-7 978-981-19-6156-4. DOI: 10.1007/978-981-19-6156-4. Accessed: May 19, 2026. [Online]. Available: https://link.springer.com/10.1007/978-981-19-6156-4.

[9] *IEEE Sweden first Historical Milestone – The Gotland HVDC Link*, 2017. Accessed: May 20, 2026. [Online]. Available: https://r8.ieee.org/sweden/2017/01/29/ieee-sweden-first-historical-milestone-the-gotland-hvdc-link/.

[10] P. Notingher, S. Hole, L. Berquez, and G. Teyssedre, "An Insight Into Space Charge Measurements," *International Journal of Plasma Environmental Science and Technology*, pp. 26–37, Nov. 2017. Accessed: Mar. 1, 2026. [Online]. Available: https://hal.science/hal-01876565/file/NotingherIJPEST2017_final.pdf.

[11] Y. Zheng, *Wave Propagation Theories and Applications*. London: IntechOpen, Feb. 2013. DOI: 10.5772/3393. Accessed: Mar. 3, 2026. [Online]. Available: https://doi.org/10.5772/3393.

[12] R. Bodega, "Space charge accumulation in polymeric high voltage DC cable systems," Dissertation (TU Delft), Delft University of Technology, 2006, ISBN: 90-8559-228-3.

[13] A. Penttinen, "Design of Pulsed Electroacoustic Measurement System for Space Charge Characterisation," M.S. thesis, Faculty of Technology, Lappeenranta University of Technology, Lappeenranta, Finland, 2012. Accessed: Mar. 1, 2026. [Online]. Available: https://lutpub.lut.fi/bitstream/handle/10024/77391/Design?sequence=1.

[14] A. Moliton, *Basic Electromagnetism and Materials*. New York, NY: Springer, 2007, ISBN: 978-0-387-30284-3.

[15] F. Aida, S. Wang, M. Fujita, G. Tanimoto, and Y. Fujiwara, "Study of the mechanism of space charge formation in polyethylene," *Journal of Electrostatics*, vol. 42, no. 1-2, pp. 3–15, Oct. 1997. Accessed: Mar. 20, 2026. [Online]. Available: https://linkinghub.elsevier.com/retrieve/pii/S0304388697001514.

[16] E. Doedens, "Topographical Impact on Space Charge Injection, Accumulation and Breakdown in Polymeric HVDC Cable Interfaces," Ph.D. dissertation, Chalmers University of Technology, 2020. Accessed: Mar. 20, 2026. [Online]. Available: https://research.chalmers.se/en/publication/519873.

[17] F. Schwabl, *Quantum Mechanics*, 4th ed. Springer-Verlag, Berlin, 2007, ISBN: 9783642091070.

[18] R. Shankar, *Principles of Quantum Mechanics*, 2nd ed. Springer, New York, 2014, ISBN: 9780306447907.

[19] N. Grigoryan, A. Roszkiewicz, and P. Chudzinski, "Generalizing Fowler-Nordheim Tunneling Theory for an Arbitrary Power Law Barrier," *Physica Status Solidi B*, pp. 1–10, Jun. 2023, 2200599, ISSN: 0370-1972, 1521-3951. Accessed: Mar. 24, 2026. [Online]. Available: http://arxiv.org/abs/2206.03722.

[20] T. A. Hoang, "Charge transport in polymer-based insulating materials for high voltage applications: Effect of single- and multi-layered structures," en, Ph.D. dissertation, Chalmers University of Technology, 2016. Accessed: Apr. 4, 2026. [Online]. Available: https://research.chalmers.se/en/publication/244812.

[21] C. Li, G. Chen, X. Qiu, Q. Lou, and X. Gao, "A direct proof for Maxwell–Wagner effect of heterogeneous interface," *AIP Advances*, vol. 11, no. 6, p. 065 227, Jun. 2021. DOI: 10.1063/5.0040947.

[22] International Electrotechnical Commission. "IEC TS 62758:2012 - Calibration of space charge measuring equipment based on the pulsed electro-acoustic

(PEA) measurement principle," Accessed: May 29, 2026. [Online]. Available: https://webstore.iec.ch/en/publication/7418.

A

Appendix 1

A.0.1 Overview of the PEA Circuit

The circuit for the PEA measurement system is presented in Figure A.1. Moreover, the circuit of the PEA can be thought of as two separate circuits in parallel: a DC circuit; and a high frequency circuit [13].

The DC circuit is comprised of a high power resistor R_{dc} in series with the resistance, R_s, of the sample. Even though the PEA cannot measure the conductivity, it is still possible to evaluate the sample resistance by

$$R_s = \frac{d}{\sigma A}, \tag{A.1}$$

where σ is the conductivity of the sample material, A and d is the area and thickness of the sample, respectively.

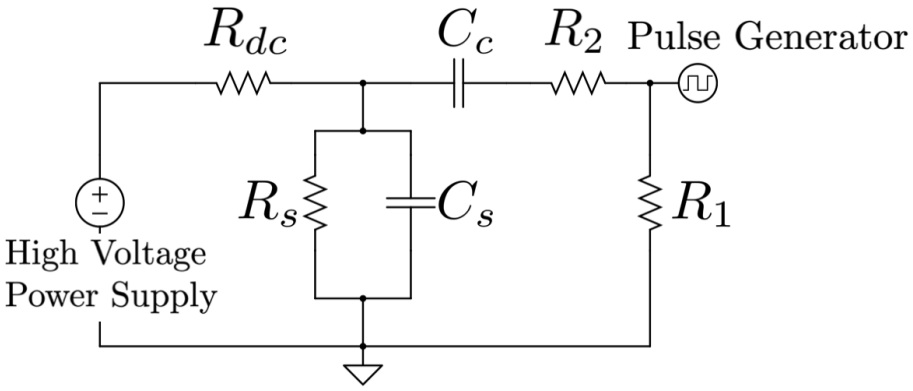

Figure A.1: PEA circuit diagram. Adapted from [13].

The two resistances R_s and R_{dc} will create a voltage divider circuit for DC signals. The DC voltage, V_s, and ultimately the static electric field, applied over the specimen will be given by

$$V_s = \left(\frac{R_s}{R_{dc} + R_s}\right) V_{dc}. \tag{A.2}$$

Since $R_s \gg R_{dc}$, the DC voltage applied of the sample can be approximated as the DC voltage from the high voltage power supply by virtue of Equation (A.2).

The main role of the high voltage resistor, R_{dc}, in the PEA circuit is to limit the short circuit current in case of an elctrical breakdown of the sample. That way, most of the power dissipates as heat through the resistor rather than in the components of the power supply [13]. In addition, it also acts blocks the high frequency pulses from the pulse generator from reaching the power supply.

The high frequency circuit is essentially a voltage divider circuit as well. The high voltage resistor, R_{dc}, can be modelled as a resistor in parallel with a capacitance C_{dc}. From the pulse generator side, the sample capacitance and the capacitance of the high power resistor will be in parallel. The capacitance of the high power resistor is much larger compared to the capacitance of the sample [13]. The capacitance of the sample can be approximated as

$$C_s = \varepsilon_0 \varepsilon_r \left(\frac{A}{d} \right), \tag{A.3}$$

where ε_0 is the permittivity of free space, ε_r is the relative permittivity of the sample, A is the area of the electrode and d is the thickness of the sample.

The effective capacitance of the capacitance of the high power resistor in parallel with the sample capacitance can be approximated as the capacitance of the high power resistor, since [13],

$$C_{eff} = C_{dc} + C_s \approx C_{dc}, \quad C_{dc} \gg C_s. \tag{A.4}$$

Therefore, most of the voltage from the pulse generator will be over the sample, depicted in Figure A.1. This can be approximated through voltage division according to the following

$$u_s = \left(\frac{Z_c}{Z_c + Z_{eff}} \right) u_p \approx \left(\frac{\frac{1}{j\omega C_c}}{\frac{1}{j\omega C_c} + \frac{1}{j\omega C_{eff}}} \right) u_p \approx \left(\frac{\frac{1}{j\omega C_c}}{\frac{1}{j\omega C_c} + \frac{1}{j\omega C_{dc}}} \right) u_p \approx u_p. \tag{A.5}$$

A.0.2 PEA Measurement Principle

Consider a dielectric sample placed in between two electrodes as illustrated in Figure A.2 subjected to a DC voltage, giving rise to a static electric field **E**. Under this DC stress space charges may accumulate within the dielectric sample [7].

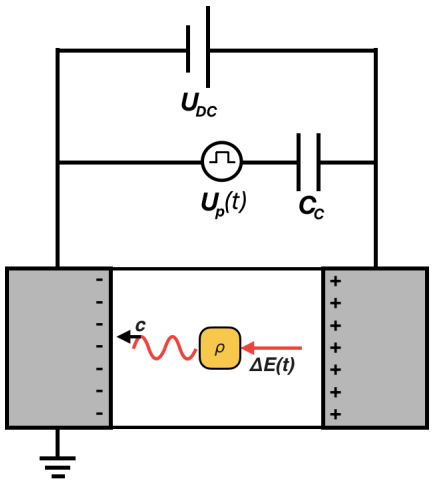

Figure A.2: Illustration depicting the pulsed field $\Delta\mathbf{E}(t)$ interacting with charge density ρ within the bulk of the sample resulting in an acoustic wave with velocity c.

To measure the charge distribution, a very short nanosecond voltage pulse, $U_p(t)$, is superimposed onto the static electric field. Each pulse creates a transient electric field $\Delta\mathbf{E}(t)$. Every local charge distribution in the material experiences an electrostatic force, $F(t)$, proportional to its charge density ρ and the pulse field $\Delta\mathbf{E}(t)$ according to [8]

$$F(t) \propto \rho\Delta\mathbf{E}(t), \tag{A.6}$$

where ρ is the local charge density and $\Delta\mathbf{E}(t)$ is the pulsed electric field. This force acts for only a few nanoseconds but it is sufficient to slightly displace the charges and compress the surrounding material. The sudden compression produces a mechanical strain in the dielectric. Because the strain changes rapidly, it will generate a pressure wave in the material. The amplitude of the generated pressure wave is proportional to the electrostatic force acting on the accumulated charge [8].

The important point is that the pressure wave is generated wherever charge exists. Charges located at the cathode electrode generate one acoustic contribution. Charges distributed throughout the bulk of the material generate many small pressure sources along the thickness of the sample.

Each pressure wave then propagates through the dielectric. The propagation speed is determined by the speed of sound, c, in the material. As the wave travels it eventually reaches the ground electrode and the piezoelectric sensor mounted behind it.

Because the propagation velocity is known the time required for the wave to reach the sensor corresponds to the position where that wave originated inside the sample [8].

B

Appendix 2

B.1 Pre-Screening Measurements of Acoustic Coupling Agents

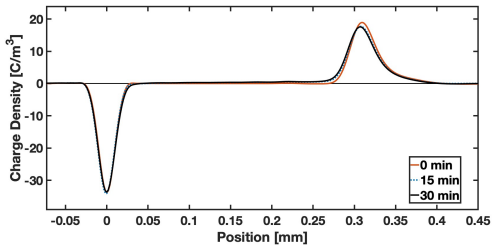

(a) Space charge profile using Oil A.

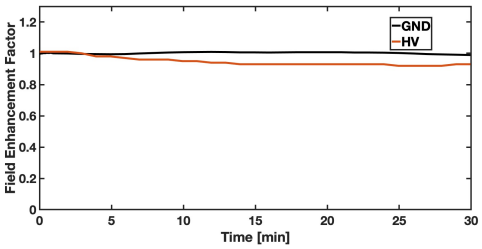

(b) Field enhancement factor using Oil A

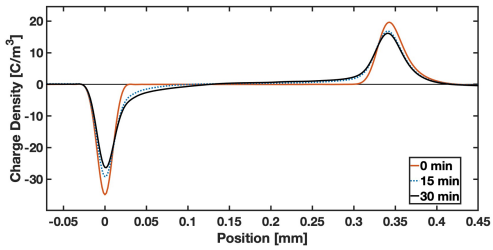

(c) Space charge profile using Oil B

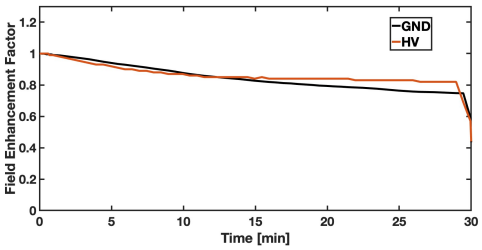

(d) Field enhancement factor using Oil B

Figure B.1: Space charge profiles and field enhancement factors obtained during pre-screening measurements performed using a DC stress of 40 kV/mm at 25 °C for 30 minutes.

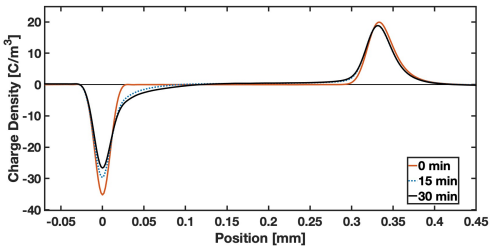

(a) Space charge profile using Oil C

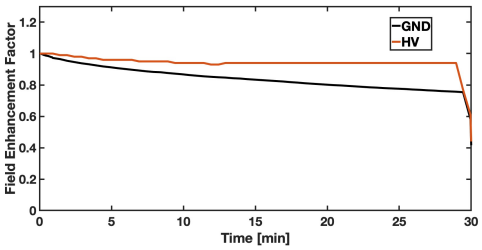

(b) Field enhancement factor using Oil C

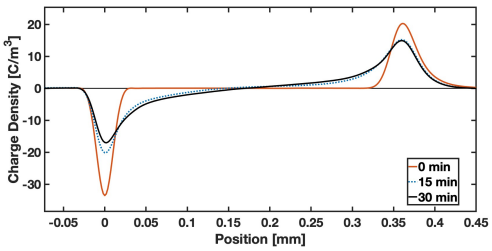

(c) Space charge profile using Oil D

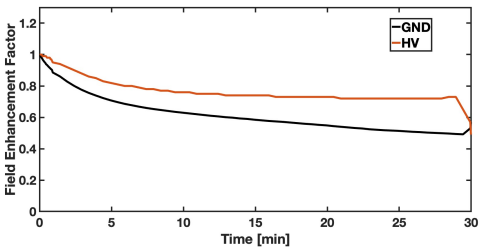

(d) Field enhancement factor using Oil D

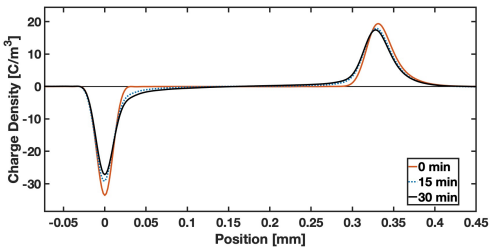

(e) Space charge profile using Oil E

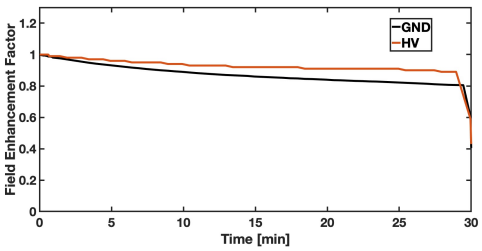

(f) Field enhancement factor using Oil E

Figure B.2: Space charge profiles and field enhancement factors obtained during pre-screening measurements performed using a DC stress of 40 kV/mm at 25 °C for 30 minutes.

C

Appendix 3

C.1 PEA Measurements

Electrode Configuration 1

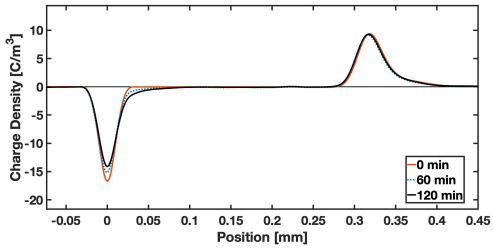

(a) Space charge profile from the first measurement.

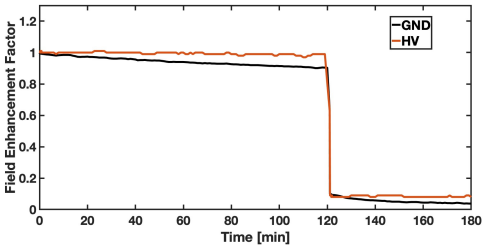

(b) Field enhancement factor from the first measurement.

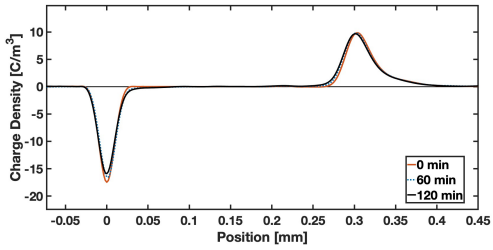

(c) Space charge profile from the second measurement.

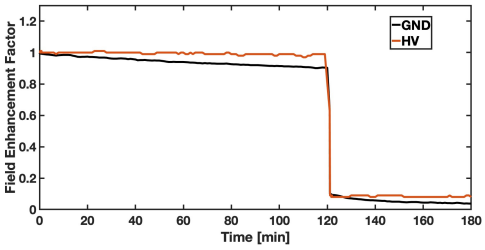

(d) Field enhancement factor from the second measurement.

Figure C.1: Space charge profiles and field enhancement factors from the two measurements performed using oil 1 with electrode configuration 1 subjected to a DC stress of 20 kV/mm at 25 °C.

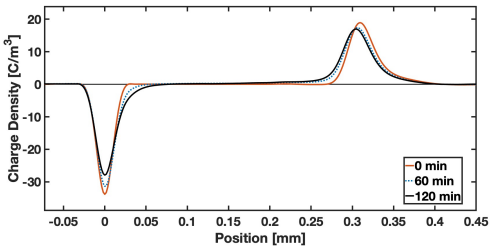

(a) Space charge profile from the first measurement.

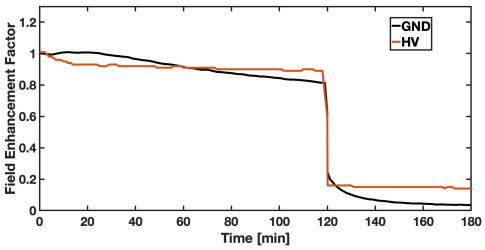

(b) Field enhancement factor from the first measurement.

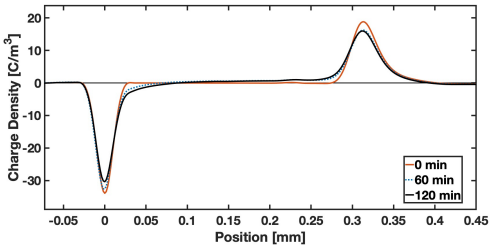

(c) Space charge profile from the second measurement.

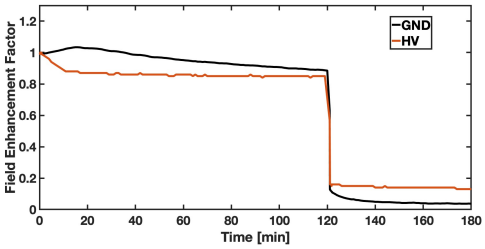

(d) Field enhancement factor from the second measurement.

Figure C.2: Space charge profiles and field enhancement factors from the two measurements performed using oil 1 with electrode configuration 1 subjected to a DC stress of 40 kV/mm at 25 °C.

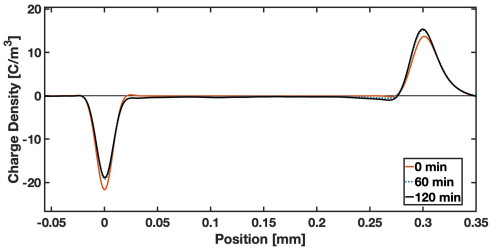

(a) Space charge profile from the first measurement.

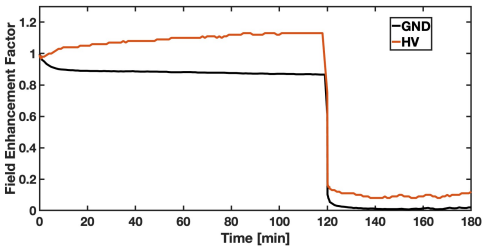

(b) Field enhancement factor from the first measurement.

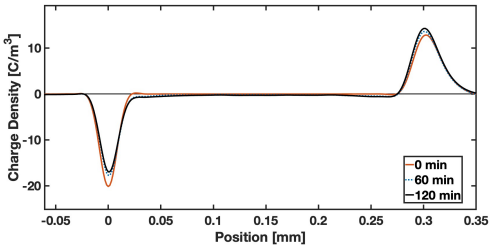

(c) Space charge profile from the second measurement.

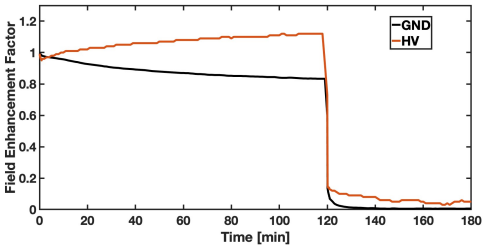

(d) Field enhancement factor from the second measurement.

Figure C.3: Space charge profiles and field enhancement factors from the two measurements performed using oil 1 with electrode configuration 1 subjected to a DC stress of 20 kV/mm at 70 °C.

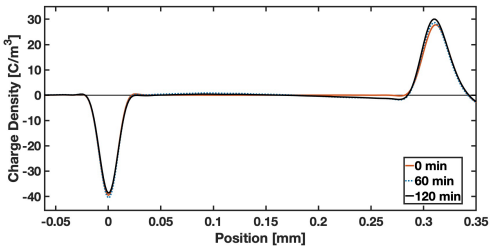

(a) Space charge profile from the first measurement.

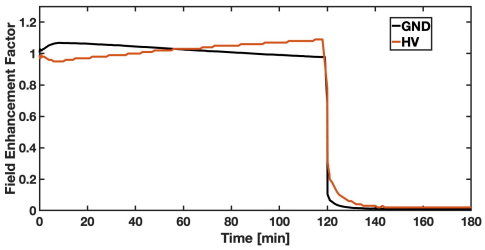

(b) Field enhancement factor from the first measurement.

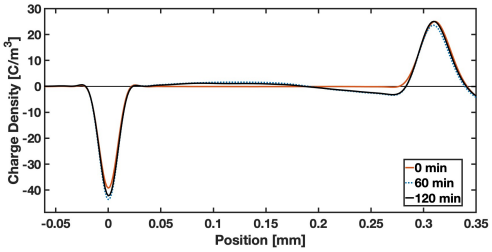

(c) Space charge profile from the second measurement.

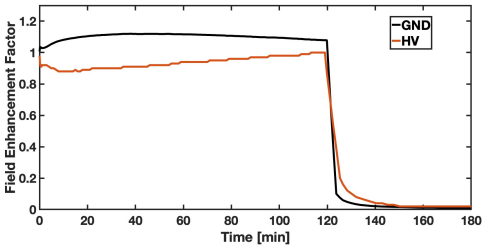

(d) Field enhancement factor from the second measurement.

Figure C.4: Space charge profiles and field enhancement factors from the two measurements performed using oil 1 with electrode configuration 1 subjected to a DC stress of 40 kV/mm at 70 °C.

Electrode Configuration 2

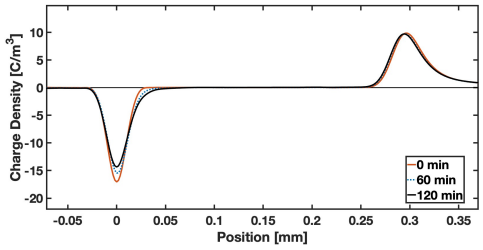

(a) Space charge profile from the first measurement.

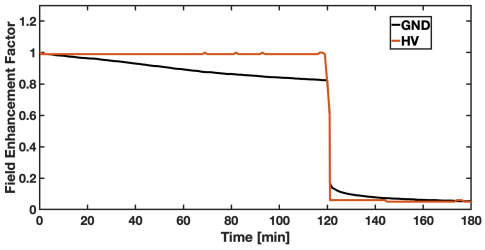

(b) Field enhancement factor from the first measurement.

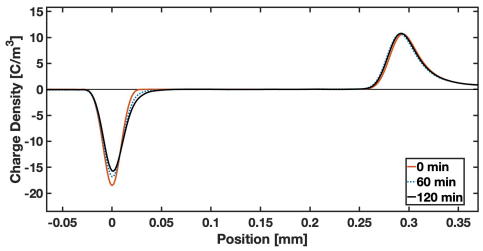

(c) Space charge profile from the second measurement.

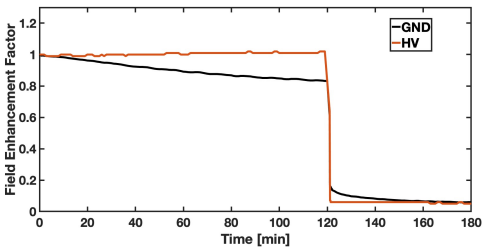

(d) Field enhancement factor from the second measurement.

Figure C.5: Space charge profiles and field enhancement factors from the two measurements performed using oil 1 with electrode configuration 2 subjected to a DC stress of 20 kV/mm at 25 °C.

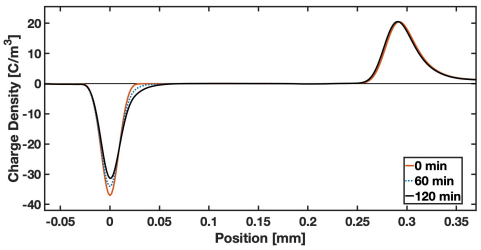

(a) Space charge profile from the first measurement.

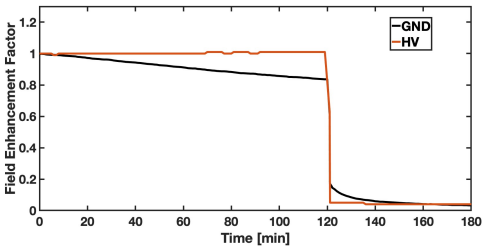

(b) Field enhancement factor from the first measurement.

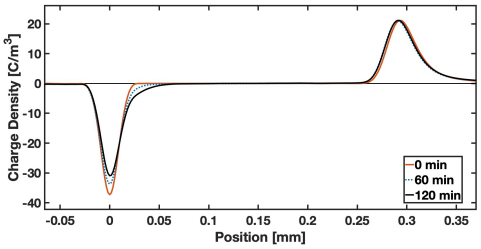

(c) Space charge profile from the second measurement.

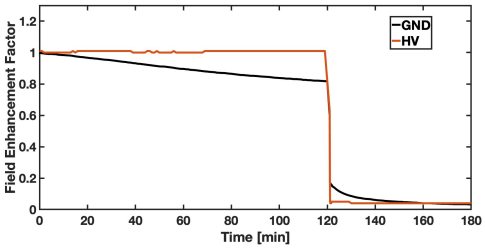

(d) Field enhancement factor from the second measurement.

Figure C.6: Space charge profiles and field enhancement factors from the two measurements performed using oil 1 with electrode configuration 2 subjected to a DC stress of 40 kV/mm at 25 °C.

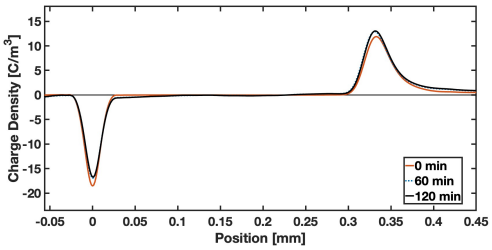

(a) Space charge profile from the first measurement.

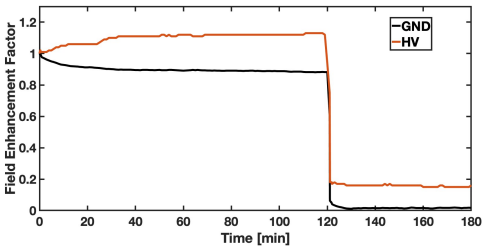

(b) Field enhancement factor from the first measurement.

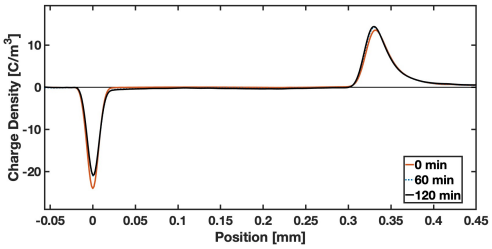

(c) Space charge profile from the second measurement.

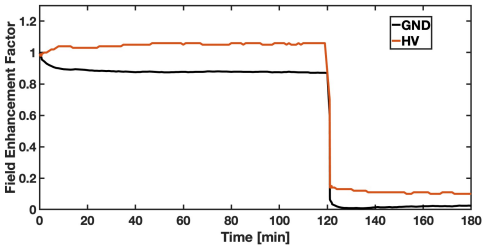

(d) Field enhancement factor from the second measurement.

Figure C.7: Space charge profiles and field enhancement factors from the two measurements performed using oil 1 with electrode configuration 2 subjected to a DC stress of 20 kV/mm at 70 °C.

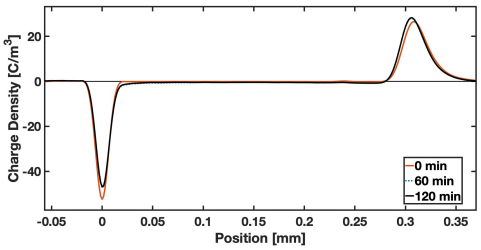

(a) Space charge profile from the first measurement.

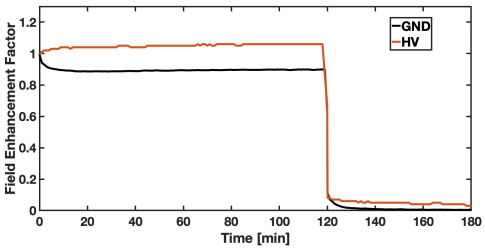

(b) Field enhancement factor from the first measurement.

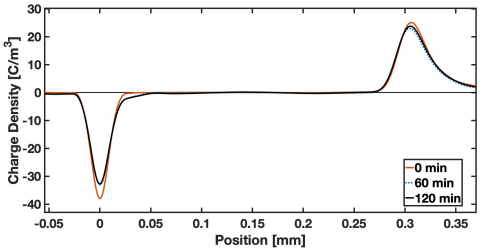

(c) Space charge profile from the second measurement.

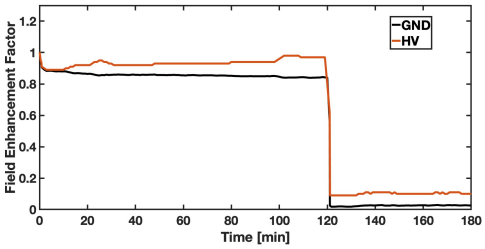

(d) Field enhancement factor from the second measurement.

Figure C.8: Space charge profiles and field enhancement factors from the two measurements performed using oil 1 with electrode configuration 2 subjected to a DC stress of 40 kV/mm at 70 °C.

Electrode Configuration 3

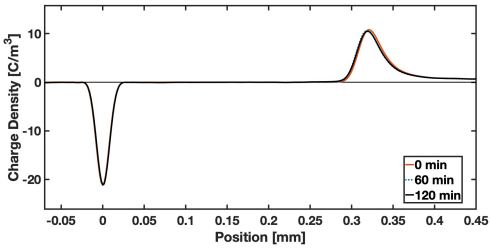

(a) Space charge profile from the first measurement.

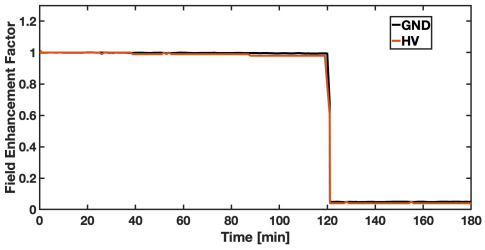

(b) Field enhancement factor from the first measurement.

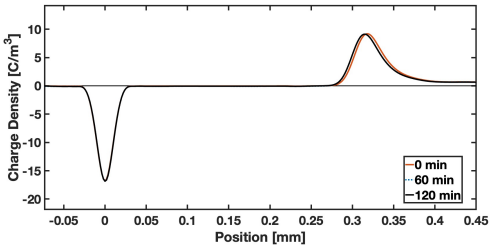

(c) Space charge profile from the second measurement.

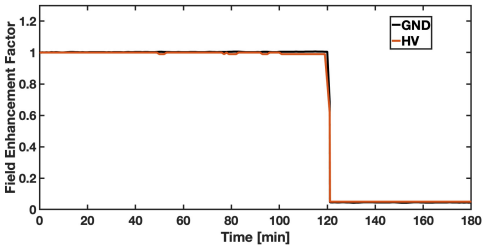

(d) Field enhancement factor from the second measurement.

Figure C.9: Space charge profiles and field enhancement factors from the two measurements performed using oil 1 with electrode configuration 3 subjected to a DC stress of 20 kV/mm at 25 °C.

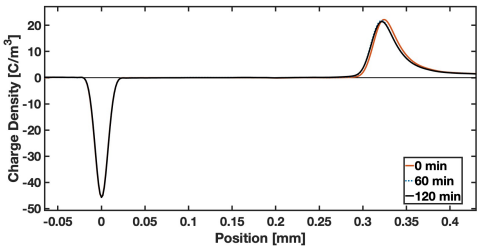

(a) Space charge profile from the first measurement.

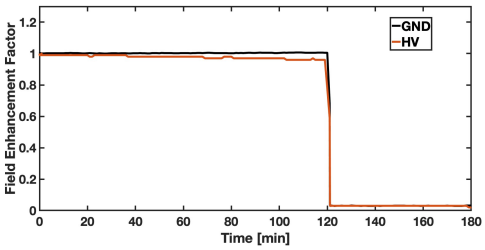

(b) Field enhancement factor from the first measurement.

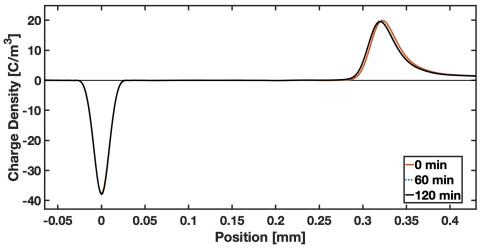

(c) Space charge profile from the second measurement.

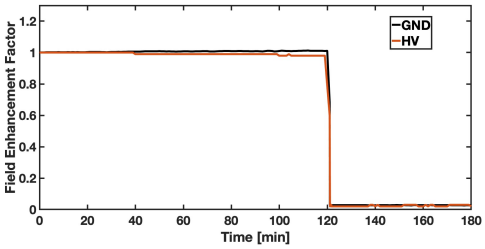

(d) Field enhancement factor from the second measurement.

Figure C.10: Space charge profiles and field enhancement factors from the two measurements performed using oil 1 with electrode configuration 3 subjected to a DC stress of 40 kV/mm at 25 °C.

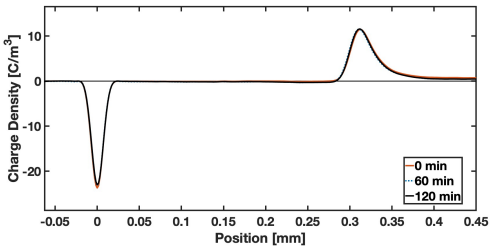

(a) Space charge profile from the first measurement.

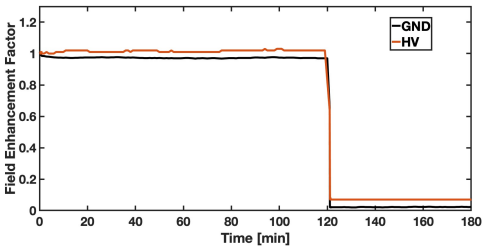

(b) Field enhancement factor from the first measurement.

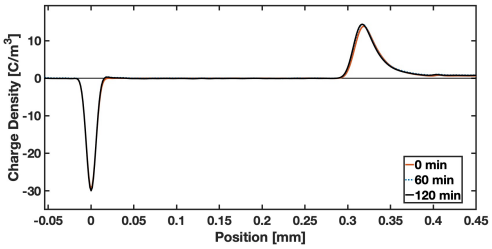

(c) Space charge profile from the second measurement.

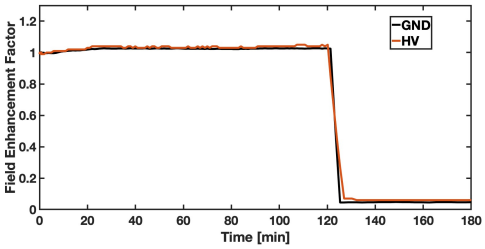

(d) Field enhancement factor from the second measurement.

Figure C.11: Space charge profiles and field enhancement factors from the two measurements performed using oil 1 with electrode configuration 3 subjected to a DC stress of 20 kV/mm at 70 °C.

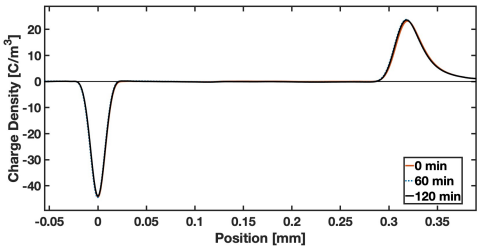

(a) Space charge profile from the first measurement.

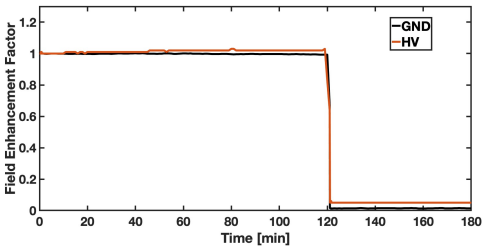

(b) Field enhancement factor from the first measurement.

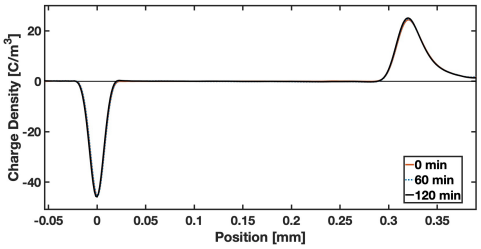

(c) Space charge profile from the second measurement.

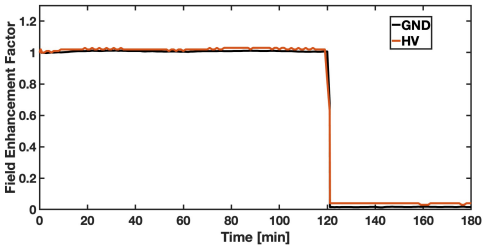

(d) Field enhancement factor from the second measurement.

Figure C.12: Space charge profiles and field enhancement factors from the two measurements performed using oil 1 with electrode configuration 3 subjected to a DC stress of 40 kV/mm at 70 °C.

Electrode Configuration 4

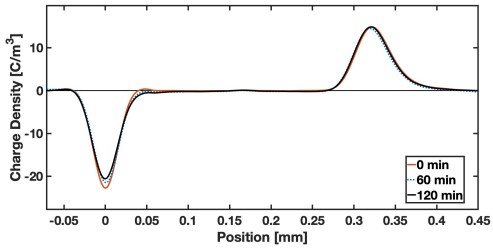

(a) Space charge profile from the first measurement.

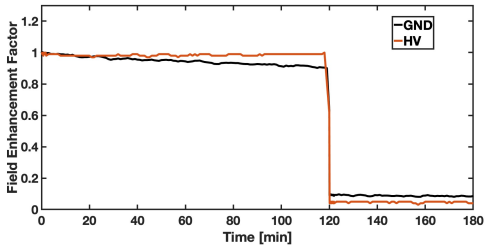

(b) Field enhancement factor from the first measurement.

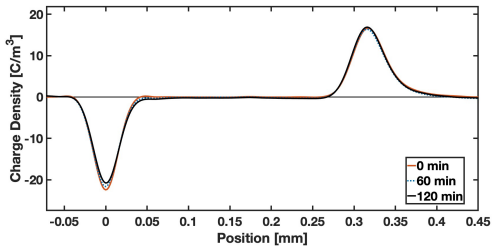

(c) Space charge profile from the second measurement.

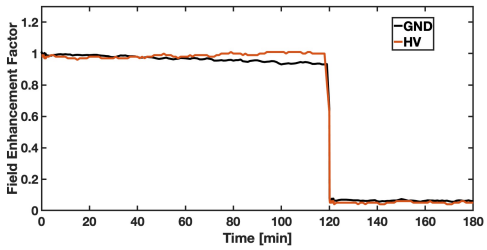

(d) Field enhancement factor from the second measurement.

Figure C.13: Space charge profiles and field enhancement factors from the two measurements performed using oil 1 with electrode configuration 4 subjected to a DC stress of 40 kV/mm at 25 °C.

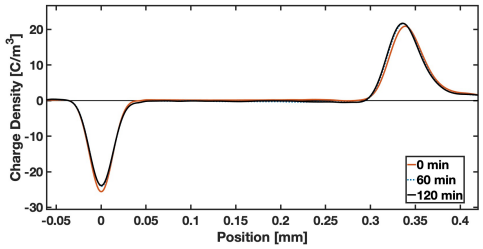

(a) Space charge profile from the first measurement

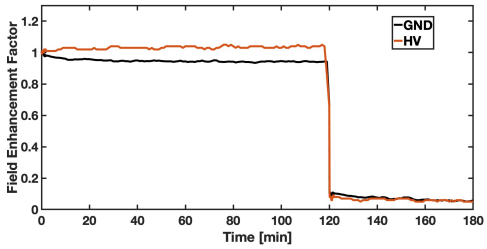

(b) Field enhancement factor from the first measurement.

Figure C.14: Space charge profile and field enhancement factor from the measurement performed using oil 1 with electrode configuration 4 subjected to a DC stress of 40 kV/mm at 70 °C.

Electrode Configuration 1 - Oil 1

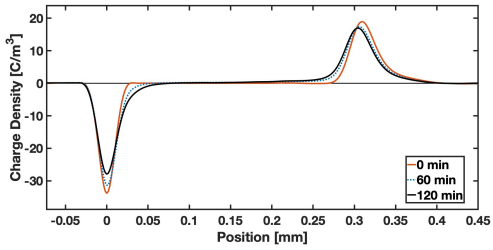

(a) Space charge profile from the first measurement.

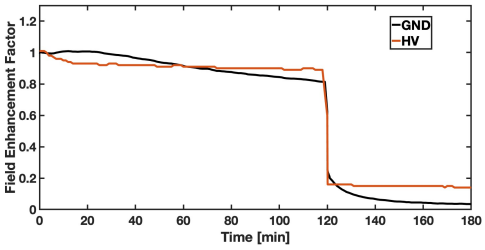

(b) Field enhancement factor from the first measurement.

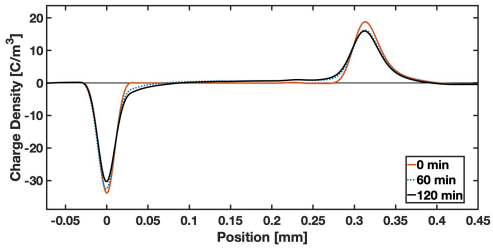

(c) Space charge profile from the second measurement.

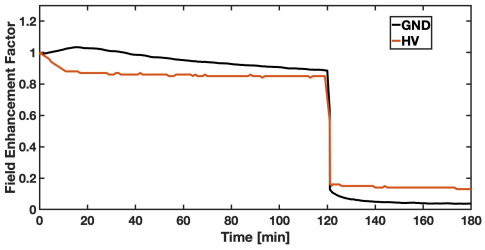

(d) Field enhancement factor from the second measurement.

Figure C.15: Space charge profiles and field enhancement factors from the two measurements performed using oil 1 with electrode configuration 1 subjected to a DC stress of 40 kV/mm at 25 °C.

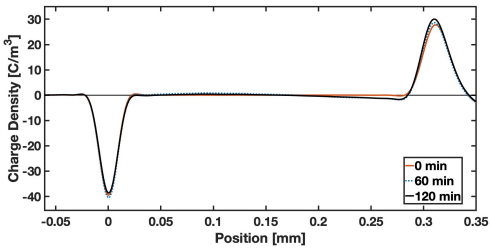

(a) Space charge profile from the first measurement.

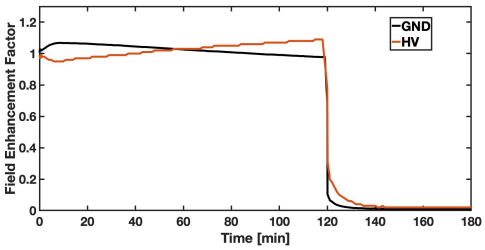

(b) Field enhancement factor from the first measurement.

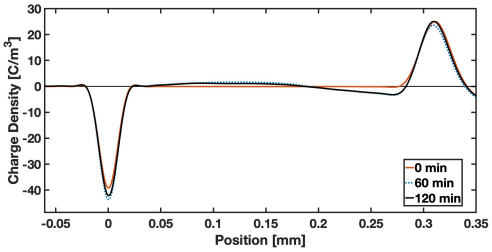

(c) Space charge profile from the second measurement.

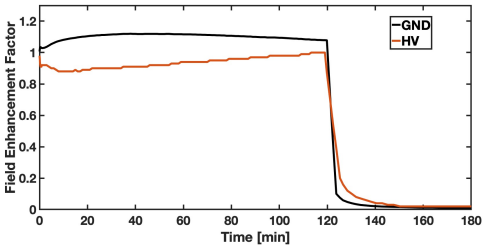

(d) Field enhancement factor from the second measurement.

Figure C.16: Space charge profiles and field enhancement factors from the two measurements performed using oil 1 with electrode configuration 1 subjected to a DC stress of 40 kV/mm at 70 °C.

Electrode Configuration 1 - Oil 2

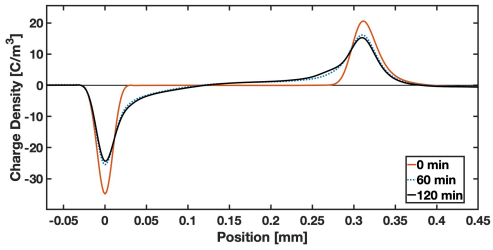

(a) Space charge profile from the first measurement.

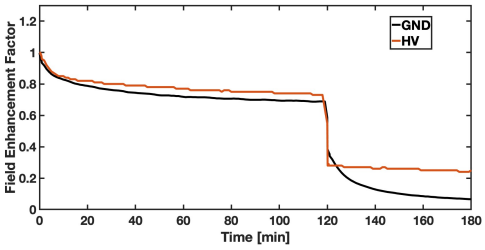

(b) Field enhancement factor from the first measurement.

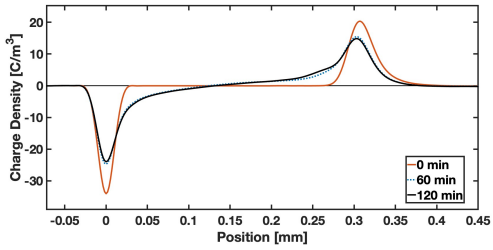

(c) Space charge profile from the second measurement.

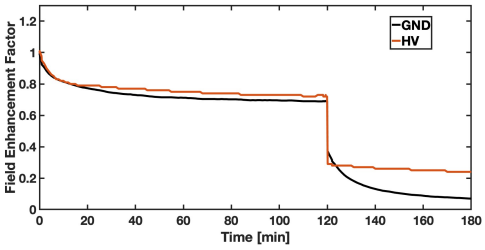

(d) Field enhancement factor from the second measurement.

Figure C.17: Space charge profiles and field enhancement factors from the two measurements performed using oil 2 with electrode configuration 1 subjected to a DC stress of 40 kV/mm at 25 °C.

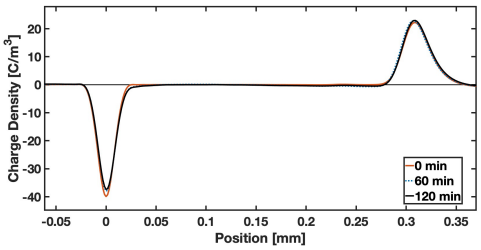

(a) Space charge profile from the first measurement.

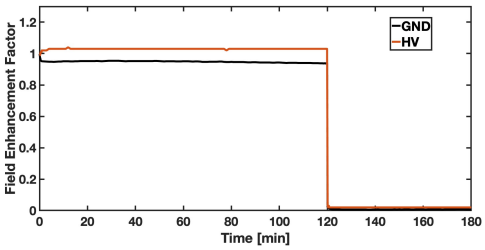

(b) Field enhancement factor from the first measurement.

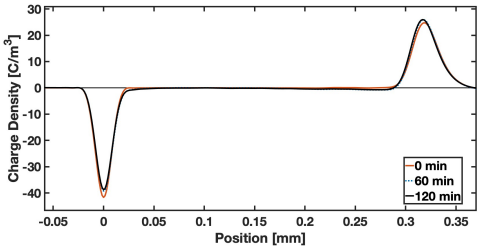

(c) Space charge profile from the second measurement.

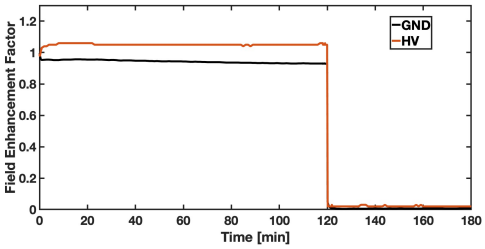

(d) Field enhancement factor from the second measurement.

Figure C.18: Space charge profiles and field enhancement factors from the two measurements performed using oil 2 with electrode configuration 1 subjected to a DC stress of 40 kV/mm at 70 °C.

Electrode Configuration 1 - Oil 3

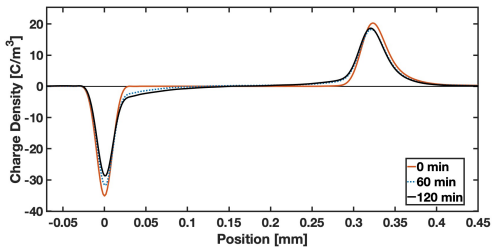

(a) Space charge profile from the first measurement.

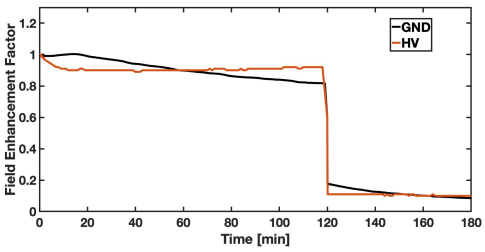

(b) Field enhancement factor from the first measurement.

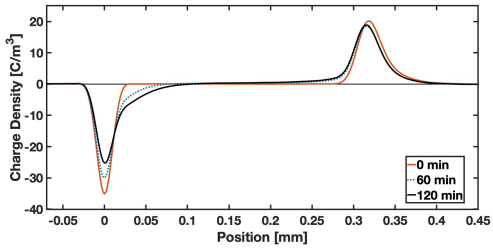

(c) Space charge profile from the second measurement.

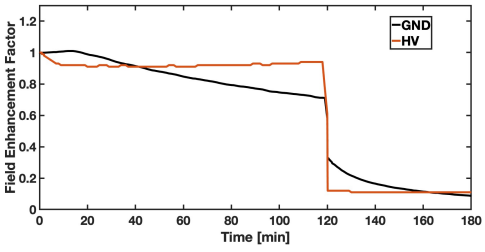

(d) Field enhancement factor from the second measurement.

Figure C.19: Space charge profiles and field enhancement factors from the two measurements performed using oil 3 with electrode configuration 1 subjected to a DC stress of 40 kV/mm at 25 °C.

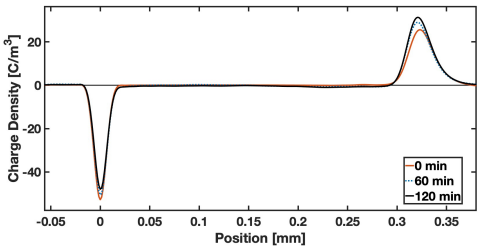

(a) Space charge profile from the first measurement.

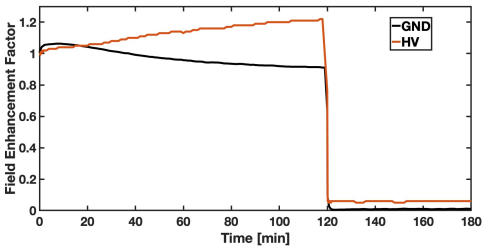

(b) Field enhancement factor from the first measurement.

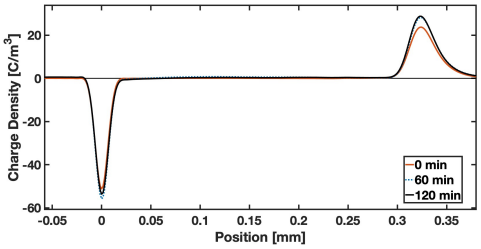

(c) Space charge profile from the second measurement.

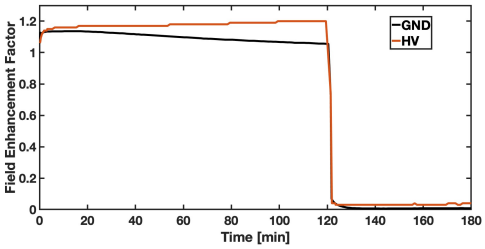

(d) Field enhancement factor from the second measurement.

Figure C.20: Space charge profiles and field enhancement factors from the two measurements performed using oil 3 with electrode configuration 1 subjected to a DC stress of 40 kV/mm at 70 °C.

Electrode Configuration 2 - Oil 1

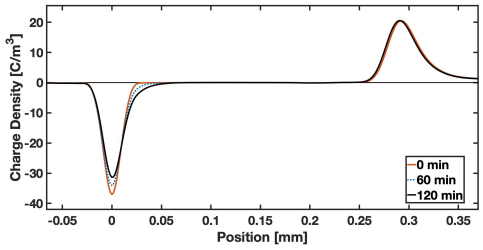

(a) Space charge profile from the first measurement.

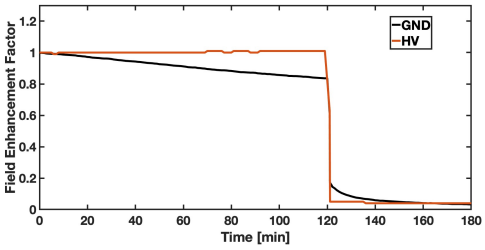

(b) Field enhancement factor from the first measurement.

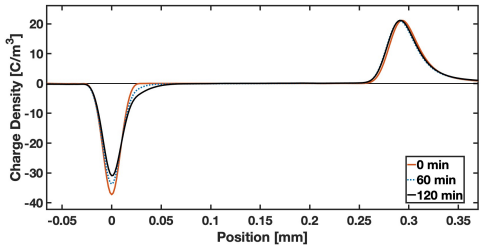

(c) Space charge profile from the second measurement.

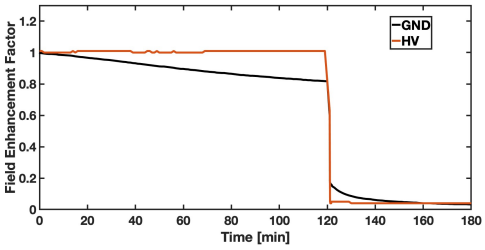

(d) Field enhancement factor from the second measurement.

Figure C.21: Space charge profiles and field enhancement factors from the two measurements performed using oil 1 with electrode configuration 2 subjected to a DC stress of 40 kV/mm at 25 °C.

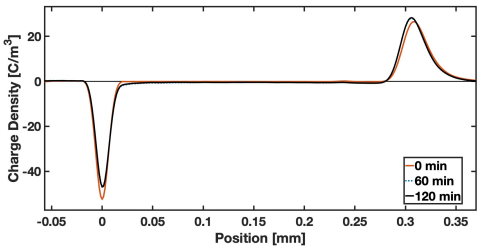

(a) Space charge profile from the first measurement.

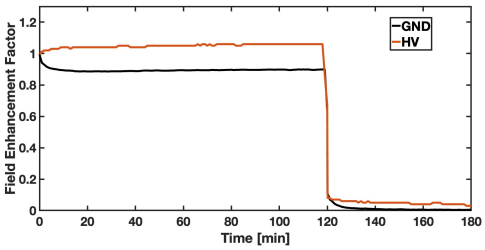

(b) Field enhancement factor from the first measurement.

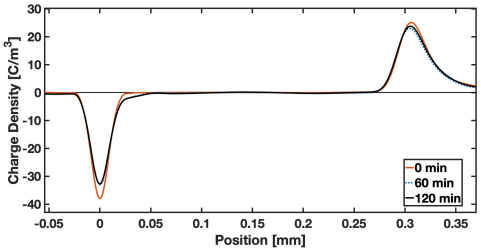

(c) Space charge profile from the second measurement.

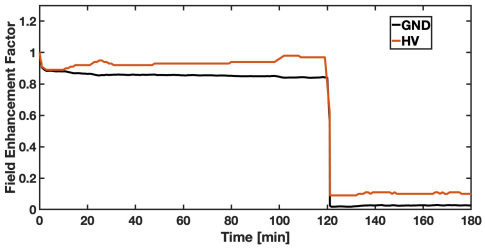

(d) Field enhancement factor from the second measurement.

Figure C.22: Space charge profiles and field enhancement factors from the two measurements performed using oil 1 with electrode configuration 2 subjected to a DC stress of 40 kV/mm at 70 °C.

Electrode Configuration 2 - Oil 2

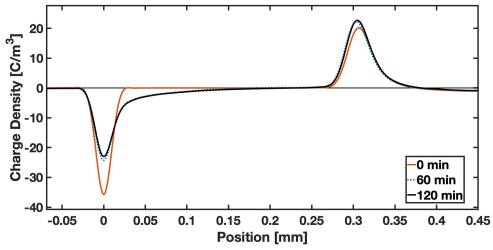

(a) Space charge profile from the first measurement.

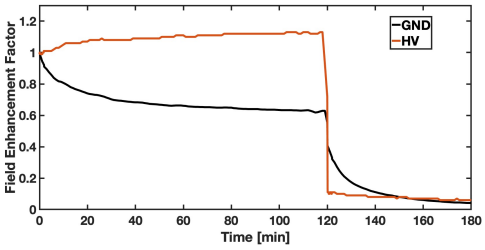

(b) Field enhancement factor from the first measurement.

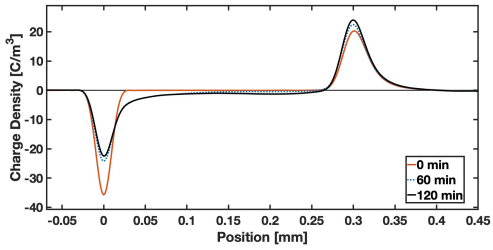

(c) Space charge profile from the second measurement.

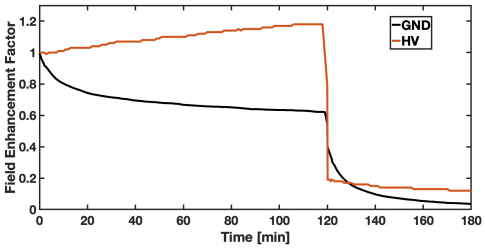

(d) Field enhancement factor from the second measurement.

Figure C.23: Space charge profiles and field enhancement factors from the two measurements performed using oil 2 with electrode configuration 2 subjected to a DC stress of 40 kV/mm at 25 °C.

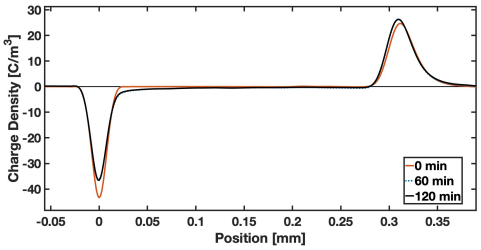

(a) Space charge profile from the first measurement.

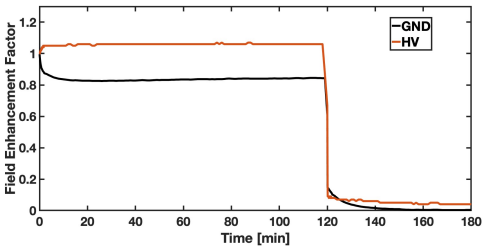

(b) Field enhancement factor from the first measurement.

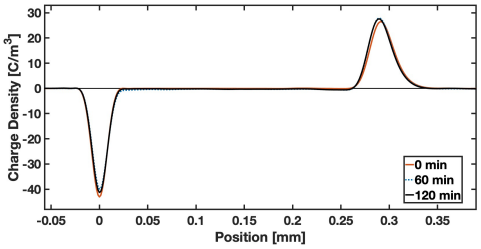

(c) Space charge profile from the second measurement.

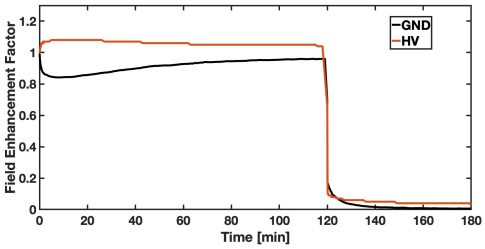

(d) Field enhancement factor from the second measurement.

Figure C.24: Space charge profiles and field enhancement factors from the two measurements performed using oil 2 with electrode configuration 2 subjected to a DC stress of 40 kV/mm at 70 °C.

DEPARTMENT OF ELECTRICAL POWER ENGINEERING
CHALMERS UNIVERSITY OF TECHNOLOGY
Gothenburg, Sweden
www.chalmers.se

CHALMERS
UNIVERSITY OF TECHNOLOGY